

pubs.acs.org/JPCA Article

# Resource Optimization for Quantum Dynamics with Tensor Networks: Quantum and Classical Algorithms

Published as part of The Journal of Physical Chemistry A virtual special issue "Gustavo Scuseria Festschrift". Anurag Dwivedi, Miguel Angel Lopez-Ruiz, and Srinivasan S. Iyengar\*



Cite This: J. Phys. Chem. A 2024, 128, 6774-6797



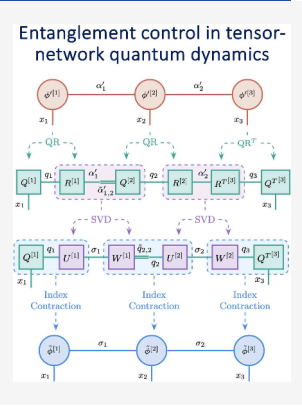
**ACCESS** I

Metrics & More

Article Recommendations

S Supporting Information

ABSTRACT: The exponential scaling of the quantum degrees of freedom with the size of the system is one of the biggest challenges in computational chemistry and particularly in quantum dynamics. We present a tensor network approach for the time-evolution of the nuclear degrees of freedom of multiconfigurational chemical systems at a reduced storage and computational complexity. We also present quantum algorithms for the resultant dynamics. To preserve the compression advantage achieved via tensor network decompositions, we present an adaptive algorithm for the regularization of nonphysical bond dimensions, preventing the potentially exponential growth of these with time. While applicable to any quantum dynamical problem, our method is particularly valuable for dynamical simulations of nuclear chemical systems. Our algorithm is demonstrated using ab initio potentials obtained for a symmetric hydrogen-bonded system, namely, the protonated 2,2'-bipyridine, and compared to exact diagonalization numerical results.



# I. INTRODUCTION

One of the most computationally challenging obstacles in simulating quantum many-body systems is the exponential scaling of the system degrees of freedom with its size.<sup>1,2</sup> The dimension of the corresponding Hilbert space is rendered so large that a complete description of an arbitrary state becomes virtually intractable. Thus, several approximation methods, have been developed that attempt to circumvent this curse of dimensionality, 3-13 with various degrees of success. For instance, one of the most powerful approaches for molecular quantum dynamics simulations is the multiconfiguration timedependent Hartree (MCTDH) method. 5,14–16 Nevertheless, it is still susceptible to the same exponential scaling issue 17,18 and early studies indicate that the multilayer MCTDH (ML-MCTDH) generalization 19,20 may avoid such a scaling issue by introducing a hierarchical Tucker decomposition 21,22 ansatz, which is a particular form of the so-called tensor network states.<sup>23,24</sup>

In this publication we discuss a computational approach for quantum dynamics that uses tensor networks and may be implementable on quantum hardware; indeed we also provide quantum circuit based algorithms to do the same. Tensor Networks (TN) are a general framework for data compression and have proven to be a very effective approach for the efficient representation of many-body quantum states in strongly correlated systems (see  $^{23,25-37}$  for comprehensive surveys). These approaches have been demonstrated for quantum dynamics  $^{18,38-51}$  and for computation of vibrational states. The tensor network methods have roots in the

tensor decomposition field of multilinear algebra <sup>21,22,56</sup> and are a central component of the work presented here. Given the advent of novel quantum computing algorithms in the literature, tensor networks are also a natural resource for developing new quantum algorithms. <sup>57–65</sup> The approach has been shown to have applications for low-energy states of local, gapped Hamiltonians which are characterized by satisfying a so-called area-law of entanglement. <sup>66–68</sup> The introduction of the density matrix renormalization group (DMRG), <sup>69–72</sup> was perhaps the catalyst for the excitement in the TN methodology; proving to be extremely useful for the simulation of one-dimensional quantum lattices, <sup>46,73,74</sup> electronic structure calculations, <sup>24,75–80</sup> approximations to vibrational states <sup>50,81–84</sup> and even machine learning applications.

Orthogonally, quantum simulations, which are based on the realization of the system degrees of freedom in question onto another quantum system with controllable parameters, are thought to be the most natural and efficient way to study large scale quantum phenomena. Nevertheless, the technological limitations of current quantum devices, have hindered the progress in this area. As we enter the era of NISQ computers, 88,89 it is crucial to develop novel quantum

Received: May 23, 2024 Revised: June 18, 2024 Accepted: June 18, 2024 Published: August 5, 2024





algorithms tailored to overcome setbacks such as, large circuit depths <sup>90,91</sup> with small number of accessible qubits, poor gate fidelity, noise reduction, and error correction. <sup>90,92–95</sup> With the emerging interest in quantum computing, the connections between TN and quantum information <sup>62–65,96–109</sup> have reignited the excitement in the field, as they are regarded as a promising tool in the development of hybrid (quantum-classical) algorithms for current and future NISQ devices. <sup>88,89,92</sup>

This paper is organized as follows. In Section II we briefly review the TN representation of the wave function as a matrix product state (MPS), followed by Section III which gives a detailed exposition of the time-evolution methodology employed to propagate such states. Connections to previous work that necessitate the development of such a protocol for, potentially, fully ab initio quantum nuclear dynamics is presented in Section III A. In Section III B, we present quantum algorithms that may be used to implement these states. The issues arising in the propagation of MPS, i.e., the exponential growth of the bond dimension, are then discussed in Section IV. In Section IV A, we introduce in a comprehensive fashion, a regularization algorithm for the bond dimension, aimed to optimize dynamical simulations of MPS. To probe and illustrate the algorithm, in Section V, we consider a symmetric short-strong hydrogen bonded system: the protonated 2,2'-bipyridine molecule. Section V A contains details of the Hamiltonian associated with this system and in Section V B we present the numerical results for the simulation of quantum dynamics with bond dimension regularization. Finally, we address our conclusions and final comments in Section VI.

# II. QUANTUM CHEMICAL DYNAMICS WITH MATRIX PRODUCT STATES

An arbitrary N-dimensional quantum state  $|\Psi\rangle\in\mathcal{H}_D^{\otimes N}$  is generally written as

$$|\Psi\rangle = \sum_{j_1, j_2, \dots, j_N}^{D} C_{j_1 j_2, \dots j_N} \bigotimes_{k=1}^{N} |j_k\rangle$$
(1)

where  $\{|j_k\rangle\}$  is a complete orthonormal basis set, one set for each dimension in  $\mathcal{H}_D^{\otimes N}$ . The computational complexity of the full description of the quantum state scales with the number of coefficients in the expansion, that is,  $\{C_{j_ij_2\cdots j_N}\}$  in eq 1. The number of elements in  $\{C_{j_ij_2\cdots j_N}\}$  scales exponentially, that is  $O(D^N)$ , which is clearly intractable for even moderate values of N. Additionally, it is useful to emphasize that eq 1 is also the starting point for MCTDH formalism. S,14–16 However, one can also write eq 1 in the position representation where the basis functions  $\{|j_k\rangle\}$  above are replaced by the coordinate representation. Thus,

$$|\Psi\rangle = \int d\mathbf{\bar{x}}\psi(\mathbf{\bar{x}}) \bigotimes_{k=1}^{N} |x_k\rangle \tag{2}$$

w h e r e  $d\overline{\mathbf{x}}\equiv dx_1dx_2\dots dx_N, \qquad \text{a n d}$   $|\overline{\mathbf{x}}\rangle\equiv |x_1\rangle|x_2\rangle\cdots|x_N\rangle\equiv\bigotimes_{k=1}^N|x_k\rangle. \text{ In the position representation, } \{|\overline{\mathbf{x}}\rangle\}, \text{ the coefficient tensor } C_{j_1j_2\dots j_N} \text{ in eq 1 becomes the wave function } \psi(\overline{\mathbf{x}})\equiv\psi_{x_1x_2\dots x_N}, \text{ and each value of } |\overline{\mathbf{x}}\rangle \text{ within this representation corresponds to a discrete grid point in spatial dimension. Indeed, this is the basis for grid-based}$ 

quantum nuclear dynamics, that has been pursued by several groups  $^{110-115}$  and is known to provide very accurate results, but at steep computational expense.  $^{8,116,117}$  Now, by performing a sequence of singular value decompositions (SVD), the *N*-order tensor  $\psi(\overline{\mathbf{x}})$  can be recast into a family of one-dimensional functions, resulting in the so-called matrix product state (MPS),  $^{48,72,118-122}$ 

$$\psi(\overline{\mathbf{x}}) = \sum_{\overline{\alpha}}^{\overline{\eta}} \phi_{\alpha_1}^{[1]x_1} \left| \prod_{j=2}^{N-1} \phi_{\alpha_{j-1}\alpha_j}^{[j]x_j} \right| \phi_{\alpha_{N-1}}^{[N]x_N}$$
(3)

In eq 3, the functional dependence on the discrete position basis  $\overline{\mathbf{x}} \equiv \{x_1, x_2, ..., x_N\}$ , is realized as tensor components labeled  $x_j$ ; hence, the order-2 and order-3 tensors  $\phi^{[j]}$  correspond to one-dimensional functions of the coordinate  $x_j$ . Notice that superscripts in squared brackets  $[\cdot]$ , are not tensor indices and are simply labels that distinguish each tensor core. The sum runs through  $\overline{\alpha} \equiv \{\alpha_1, \alpha_2, ..., \alpha_{N-1}\}$  with respective limits  $\overline{\eta} \equiv \{\eta_1, \eta_2, ..., \eta_{N-1}\}$ , commonly named entanglement dimension, bond dimension, or Schmidt rank. Each  $\eta_j$  is defined as the number of nonzero singular values resulting from the Schmidt decomposition of each bipartite subsystem created in the construction of the tensor network. For ease of notation, the resulting left and right singular vectors of the SVDs, have been rescaled by their neighboring singular values  $\lambda^{[j]}$  as follows:

$$\phi_{\alpha_1}^{[1]x_1} \sqrt{\lambda_{\alpha_1}^{[1]}} \to \phi_{\alpha_1}^{[1]x_1}$$
 (4a)

$$\sqrt{\lambda_{\alpha_{j-1}}^{[j-1]}} \phi_{\alpha_{j-1}\alpha_{i}}^{[j]x_{j}} \sqrt{\lambda_{\alpha_{j}}^{[j]}} \rightarrow \phi_{\alpha_{j-1}\alpha_{j}}^{[j]x_{j}}$$

$$\tag{4b}$$

$$\sqrt{\lambda_{a_N}^{[N]}} \phi_{a_N}^{[N]x_N} \to \phi_{a_N}^{[N]x_N} \tag{4c}$$

The TN methods allow a diagrammatic notation for complex tensor representations and operations and in Figure 1 we show the corresponding TN diagram of eq 3.

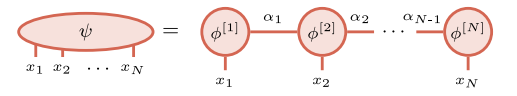


**Figure 1.** TN diagram of the MPS factorization of the wave function  $\psi(\overline{\mathbf{x}};t)$ . The order-N tensor  $\psi$ , comprised of the coefficients defining the quantum state  $|\psi\rangle$  in the discrete position basis, is factorized into a product of N order-3 tensors. By convention, in diagrammatic notation, TN are represented as graphs where the tensor cores are depicted as nodes, "free indices" are shown as open edges, while connected edges correspond to "dummy" or contracted indices.

In addition to storage of the wave function, a key challenge in quantum dynamics involves the action of the time-evolution operator on some state vector:  $\hat{U}|\Psi\rangle$ . Toward this, we use a Matrix Product Operator (MPO)<sup>123</sup> to propagate the MPS, that is,

$$\langle \overline{\mathbf{x}}' | \hat{U} | \overline{\mathbf{x}} \rangle \equiv \sum_{\overline{\beta}} \mathcal{U}_{\beta_{1}}^{[1]x_{1}x'_{1}} \left[ \prod_{j=2}^{N-1} \mathcal{U}_{\beta_{j-1}\beta_{j}}^{[j]x_{j}x'_{j}} \right] \mathcal{U}_{\beta_{N-1}}^{[N]x_{N}x'_{N}}$$
(5)

where, the sum runs through the entanglement variables  $\overline{\beta} \equiv \{\beta_1, \beta_2, ..., \beta_{N-1}\}$ , and hence,

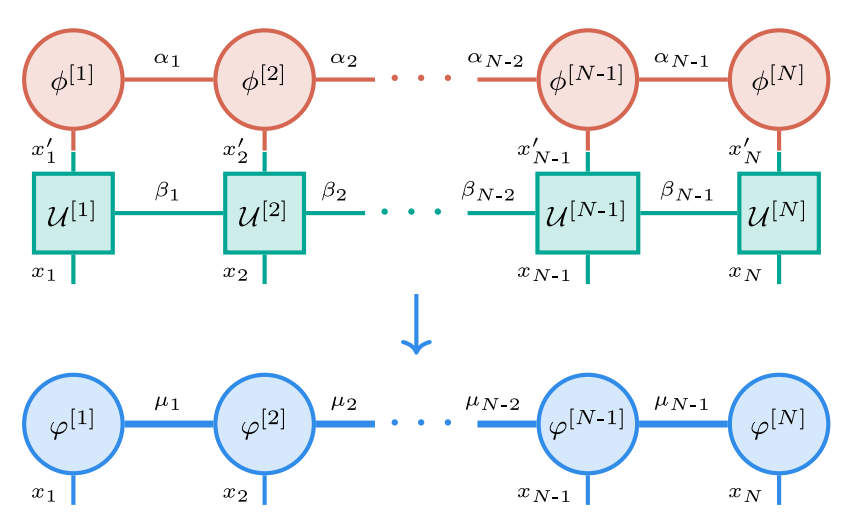


Figure 2. Action of the time evolution operator onto the MPS wave function shown in eq 17. Whereas the initial vector is given by entanglement variables  $\overline{\alpha}$ , the propagator in eq 5 has entanglement variables,  $\overline{\beta}$ , which combine to determine the index  $\overline{\mu} \equiv {\{\overline{\alpha}, \overline{\beta}\}}$  for the propagated system; shown here as a thicker edge to emphasize its larger size.

$$\hat{U}|\Psi\rangle \rightarrow \int d\overline{x}' \sum_{\overline{\alpha},\overline{\beta}} (\mathcal{U}_{\beta_{1}}^{[1]x_{1}x_{1}'} \phi_{\alpha_{1}}^{[1]x_{1}'}) \prod_{j=2}^{N-1} (\mathcal{U}_{\beta_{j-1}\beta_{j}}^{[j]x_{j}'} \phi_{\alpha_{j-1}\alpha_{j}}^{[j]x_{j}'}) 
\times (\mathcal{U}_{\beta_{N-1}}^{[N]x_{N}x_{N}'} \phi_{\alpha_{N-1}}^{[N]x_{N}'}) 
= \sum_{\overline{\alpha},\overline{\beta}} \int dx_{1}' (\mathcal{U}_{\beta_{1}}^{[1]x_{1}x_{1}'} \phi_{\alpha_{1}}^{[1]x_{1}'}) 
\times \prod_{j=2}^{N-1} \int dx_{j}' (\mathcal{U}_{\beta_{j-1}\beta_{j}}^{[j]x_{j}x_{j}'} \phi_{\alpha_{j-1}\alpha_{j}}^{[j]x_{j}'}) 
\times \int dx_{N}' (\mathcal{U}_{\beta_{N-1}}^{[N]x_{N}x_{N}'} \phi_{\alpha_{N-1}}^{[N]x_{N}'})$$
(6)

as depicted in Figure 2. The result is a family of reduced dimensional propagated vectors,

$$\begin{split} \left\{ \int \mathrm{d}x_{1}' \mathcal{U}_{\beta_{1}}^{[1]x_{1}x_{1}'} \phi_{\alpha_{1}}^{[1]x_{1}'}, \, \cdots, \, \int \mathrm{d}x_{j}' \mathcal{U}_{\beta_{j-1}\beta_{j}}^{[j]x_{j}x_{j}'} \phi_{\alpha_{j-1}\alpha_{j}}^{[j]x_{j}'}, \, \cdots \\ \cdots, \, \int \mathrm{d}x_{N}' \, \mathcal{U}_{\beta_{N-1}}^{[N]x_{N}x_{N}'} \phi_{\alpha_{N-1}}^{[N]x_{N}'} \right\} \end{split}$$

as seen from the bottom (blue colored) tensors in Figure 2:

$$\hat{U}|\Psi\rangle = \sum_{\overline{\alpha},\overline{\beta}} \varphi_{\alpha_{1},\beta_{1}}^{[1]x_{1}} \left| \prod_{j=2}^{N-1} \varphi_{\alpha_{j-1},\alpha_{j},\beta_{j-1},\beta}^{[j]x_{j}} \right| \varphi_{\alpha_{N-1},\beta_{N-1}}^{[N]x_{N}}$$

$$= \sum_{\overline{\mu}} \varphi_{\mu_{1}}^{[1]x_{1}} \left| \prod_{j=2}^{N-1} \varphi_{\mu_{j-1},\mu_{j}}^{[j]x_{j}} \right| \varphi_{\mu_{N-1}}^{[N]x_{N}} \tag{8}$$

II.A. Current Approaches to Quantum Propagation. Operator splitting of unitary operators has been well-known in numerical solutions to differential equations  $^{124}$  and hence also for the Schrödinger equation.  $^{125-127}$  A few powerful approaches to represent the action  $\hat{U}|\Psi\rangle$  include: (a) the use of fast Fourier transforms  $^{126,128-132}$  to efficiently compute the momentum representation of wave functions where the free-propagator is diagonal, (b) the use of direct or iterative, Lanczos based diagonalization of the full Hamiltonian and subsequent representation of the evolution operator

 $\hat{U}(t) = \exp[-i\hat{H}t/\hbar]$  using critical eigenstates, (c) the use of Chebychev polynomial approximations 8,9,133-136 based on the Jacobi-Anger formula, 137 and (d) the use of Feynman path integration. 138-141 The list here is not exhaustive and a detailed discussion on the topic may be found in refs11, 110. The problem of time-evolving a wave function in MPS form has led to the development of several other numerical methods (see 50,142,143 for a review), which essentially fall into two main categories. These include methods based on the approximation of the unitary operator  $\hat{U}(t)$ , followed by its direct application to the MPS in question (e.g., time-evolving block decimation (TEBD), 144–146 Tensor-Train Split-Operator Fourier Transform (TT-SOFT), 45 or the MPO W<sup>I,II</sup> method 147). On the other hand, there are those that approximate the propagated state itself, that is, without the explicit computation of  $\hat{U}(t)$ (e.g., Lanczos-based Krylov subspace methods, 148-151 Chebyshev method (FTTC). 9,136,152-155 Perhaps one of the most general approaches for quantum time-evolution utilizes the Dirac-Frenkel Time-Dependent Variational Principle  $(TDVP)^{46,47,156-159}$ ).

It is also worth noting the connections and differences between the tensor-network propagation method and the previously mentioned MCTDH approaches. First, the wave function ansatz in both methodologies are similarly expressed using tensor network decompositions: Tucker format for MCTDH, 5,14-16 hierarchical Tucker format (also known as tree tensor network) in ML-MCTDH, 19,20 and recently an MPS formulation of MCTDH was developed in ref 160. Nevertheless, the principal differences between both methodologies lies in the mechanisms to simulate quantum dynamics. MCTDH methods are based on the Dirac-Frenkel timedependent variational principle which lead to the nonlinear equations of motion of the variational coefficients and singleparticle orbitals defined in the ansatz. On the other hand, as it will be discussed thoroughly in the next section, in the approach we follow here, the dynamics are carried out by representing the time-evolution operator in a convenient TN format, allowing its direct application to the MPS ansatz. Additionally, the POTFIT method<sup>161–164</sup> for potential energy surface representation is a significant step in improving the computational efficiency for the multilayer form of MCTDH

(ML-MCTDH). <sup>5,19</sup> In POTFIT, the potential energy surface which determines the unitary in eq 5 is expanded as a sum of product, <sup>161,165</sup> but the associated expansion <sup>17</sup> retains the exponential scaling complexity of the problem. The computational prefactor is reduced in POTFIT by choosing the single-particle basis functions in a careful manner. <sup>161</sup> Furthermore, reduced scaling options are also available by carefully choosing the off-diagonal elements of  $\psi_{j_1j_2...j_N}$  in eq 1 as a product of the relevant diagonal terms, <sup>165</sup> that is  $\psi_{j_1j_2...j_N} \equiv \Pi_i\psi_{j_i}$  in ref 165. Within this context the POTFIT approach has been further improved through a multilayer representation <sup>17</sup> where dimensions are coupled together in a logical fashion to achieve a tree-like architecture that captures the "local" correlation to reduce the complexity of storage associated with wave function and propagation.

# III. GENERAL PRESCRIPTIONS FOR A PARTITIONED QUANTUM DYNAMICS SCHEME ON AN MPS STATE

In the discrete coordinate representation,  $\{|\overline{\mathbf{x}}\rangle\}$ , noted in eq 2, the matrix elements of the nuclear Hamiltonian, with corresponding time-evolution operator given by eq 6, have the general form

$$\langle \overline{\mathbf{x}}' | \hat{H} | \overline{\mathbf{x}} \rangle = K(\overline{\mathbf{x}}', \overline{\mathbf{x}}) + V(\overline{\mathbf{x}}) \prod_{j=1}^{N} \delta_{x_{j}'}^{x_{j}}$$
(9)

where K is the kinetic energy and  $V(\overline{\mathbf{x}})$  is the multidimensional potential energy operator that is local in the coordinate representation. This local, time-independent, effective potential is obtained from the electronic structure.

There exist several approximations to the time-evolution operator  $^{8,9,131,136}_{}$  and associated Green's functions,  $^{8,136}_{}$  including the commonly used Trotter-Suzuki factorization,  $^{125,127,166-169}_{}$  where the latter enables a straightforward approximation of the operator, with an accuracy dependent on the time-step size  $\Delta t$ . The Trotter symmetric split operator  $^{125,127}_{}$  expansion of  $\hat{U}(\Delta t)$ , at second order in  $\Delta t$ , is given by

$$e^{-i\hat{H}\Delta t/\hbar} = e^{-i\hat{V}\Delta t/2\hbar} e^{-i\hat{K}\Delta t/\hbar} e^{-i\hat{V}\Delta t/2\hbar} + O(\Delta t^3)$$
 (10)

It must be noted that electronic structure based potential surface calculation,  $\hat{V}$ , in itself has exponential scaling computational complexity. Assuming N nuclear dimensions to be treated quantum mechanically with D discretizations per quantum nuclear dimension, leads to a total of  $D^N$  discretizations, and hence electronic structure calculations, to define the entire potential energy surface. We have recently shown that molecular fragmentation can be used to generate a potential surface propagator in tensor network form for cost that is much more favorable. Total A brief discussion of this aspect is presented in Section III A. In this paper though, we

represent the potential energy components of the Trotterized operator in the discrete position basis as

$$e^{-i\hat{V}\Delta t/2\hbar} = \sum_{\overline{\mathbf{x}},\overline{\mathbf{x}}'} \mathcal{V}_{x_1\dots x_N}^{x_1'\dots x_N'} |x_1\dots x_N\rangle\langle x_1'\dots x_N'|$$
(11)

where we have tersely assumed a  $\Delta t$ -dependence to the highorder tensor  $\mathcal{V}$ . The MPO representation of the coefficient tensor  $\mathcal{V}$  in eq 11, is obtained by the matrix product expansion,

$$\mathcal{V}_{x_{1}...x_{N}}^{x_{1}'...x_{N}'} = \sum_{\overline{\beta}} \mathcal{V}_{\beta_{1}}^{[1]x_{1}'x_{1}} \left[ \prod_{j=2}^{N-1} \mathcal{V}_{\beta_{j-1}\beta_{j}}^{[j]x_{j}'x_{j}} \right] \mathcal{V}_{\beta_{N-1}}^{[N]x_{N}'x_{N}}$$
(12)

Since the potential energy operator  $\hat{V}$  is local, it is diagonal when expressed in the position basis. Thus, the functional representation of the potential propagator, analogous to eq 3, is reduced to

$$\langle \overline{\mathbf{x}}' | \mathbf{e}^{-i\hat{V}\Delta t/2\hbar} | \overline{\mathbf{x}} \rangle = \mathbf{e}^{-iV(\overline{\mathbf{x}})\Delta t/2\hbar} \prod_{j=1}^{N} \delta_{x_{j}'}^{x_{j}}$$

$$= \sum_{\overline{\beta}} \mathcal{V}_{\beta_{1}}^{[1]x_{1}} \left[ \prod_{j=2}^{N-1} \mathcal{V}_{\beta_{j-1}\beta_{j}}^{[j]x_{j}} \right] \mathcal{V}_{\beta_{N-1}}^{[N]x_{N}}$$
(13)

where repeated indices (such as  $x_j'x_j\delta_{x_j'}^{x_j}$  in eq 12) are omitted for simplicity; leaving the propagator with the same degrees of freedom as those of an MPS. (Compare eqs 3 and 13.)

On the other hand, because the kinetic energy operator is separable across each spatial variable in coordinate representation, the kinetic propagator  $\langle \mathbf{x}'|\exp(-i\hat{K}\Delta t/\hbar)|\mathbf{x}\rangle$ , can thus be exactly factorized into a product of one-dimensional propagators, of the form

$$\langle \overline{\mathbf{x}}' | \mathbf{e}^{-i\hat{K}\Delta t/\hbar} | \overline{\mathbf{x}} \rangle = \prod_{j=1}^{N} \langle x_j' | \mathbf{e}^{-i\hat{K}_j \Delta t/\hbar} | x_j \rangle$$

$$\equiv \prod_{j=1}^{N} \mathcal{K}_{x_j'}^{[j]x_j}$$
(14)

where the direct product of the lower dimensional free-propagators,  $\mathcal{K}_{x_j'}^{[j]x_j} \equiv \mathcal{K}^{[j]}(x_j, x_j')$ , leads to the full-dimensional free-propagator in orthogonal coordinate systems. <sup>172</sup>

Finally, the time-evolution of the MPS nuclear wave function of eq 3 is obtained by combining eqs 10, 13, and 14. But in doing so we recognize that this propagation can be divided into many portions. Specifically, the free-propagator does not couple dimensions and acts on one dimension at a time. Additionally, the MPS form of the potential propagator in eq 13, also has a sum of product form, where each product acts in parallel on each separated dimension. Therefore,

$$\psi(\overline{\mathbf{x}}; t + \Delta t) \equiv \int d\overline{\mathbf{x}}' \langle \overline{\mathbf{x}} | e^{-i\hat{H}\Delta t/\hbar} | \overline{\mathbf{x}}' \rangle \psi(\overline{\mathbf{x}}'; t) 
= \int d\overline{\mathbf{x}}' \sum_{\overline{\alpha}, \overline{\beta}, \overline{\gamma}} (\mathcal{V}_{\gamma_{1}}^{[1]x_{1}} \mathcal{K}_{x_{1}'}^{[1]x_{1}} \mathcal{V}_{\beta_{1}}^{[1]x_{1}'}) \phi_{\alpha_{1}}^{[1]x_{1}'} \left[ \prod_{j=2}^{N-1} (\mathcal{V}_{\gamma_{j-1}i_{j}}^{[j]x_{j}} \mathcal{K}_{x_{j}'}^{[j]x_{j}} \mathcal{V}_{\beta_{j-1}\beta_{j}}^{[j]x_{j}'}) \phi_{\alpha_{j-1}\alpha_{j}}^{[j]x_{j}'} \right] (\mathcal{V}_{\gamma_{N-1}}^{[N]x_{N}} \mathcal{K}_{x_{N}'}^{[N]x_{N}} \mathcal{V}_{\beta_{N-1}}^{[N]x_{N}'}) \phi_{\alpha_{N-1}}^{[N]x_{N}'}$$
(15)

where we emphasize the partitioned nature of the quantum propagator, arising from the use of eqs 10, 13, and 14. This

also allows us to construct a family of one-dimensional quantum propagation steps according to

$$\psi(\overline{\mathbf{x}}; t + \Delta t) = \sum_{\overline{\alpha}, \overline{\beta}, \overline{\gamma}} \left[ \int dx'_{1} (\mathcal{V}_{\gamma_{1}}^{[1]x_{1}} \mathcal{K}_{x'_{1}}^{[1]x_{1}} \mathcal{V}_{\beta_{1}}^{[1]x'_{1}}) \phi_{\alpha_{1}}^{[1]x'_{1}} \right] \left[ \int dx'_{2} (\mathcal{V}_{\gamma/2}^{[2]x_{2}} \mathcal{K}_{x'_{2}}^{[2]x_{2}} \mathcal{V}_{\beta_{1}\beta_{2}}^{[2]x'_{2}}) \phi_{\alpha_{1}\alpha_{2}}^{[2]x'_{2}} \right] ...$$

$$\times ... \left[ \int dx'_{N-1} (\mathcal{V}_{\gamma_{N-2}\gamma_{N-1}}^{[N-1]x_{N-1}} \mathcal{K}_{x'_{N-1}}^{[N-1]x_{N-1}} \mathcal{V}_{\beta_{N-2}\beta_{N-1}}^{[N-1]x'_{N-1}}) \phi_{\alpha_{N-2}\alpha_{N-1}}^{[N-1]x'_{N-1}} \right] \left[ \int dx'_{N} (\mathcal{V}_{\gamma_{N-1}}^{[N]x_{N}} \mathcal{K}_{x'_{N}}^{[N]x_{N}} \mathcal{V}_{\beta_{N-1}}^{[N]x'_{N}}) \phi_{\alpha_{N-1}}^{[N]x'_{N}} \right]$$
(16)

and finally

$$\psi(\overline{\mathbf{x}}; t + \Delta t) = \sum_{\overline{\mu}} \varphi_{\mu_1}^{[1]x_1} \varphi_{\mu_1 \mu_2}^{[2]x_2} \dots \varphi_{\mu_{N-2} \mu_{N-1}}^{[N-1]x_{N-1}} \varphi_{\mu_{N-1}}^{[N]x_N}$$
(17)

where we have introduced the tensor index,  $\overline{\mu} \equiv \{\overline{\alpha}, \overline{\beta}, \overline{\gamma}\}$ , which is in turn defined by the "index fusion" operation  $\alpha_i \beta_j \gamma_k > \mu_n$  and so on. The essence of eq 17 is captured in Figure 3.

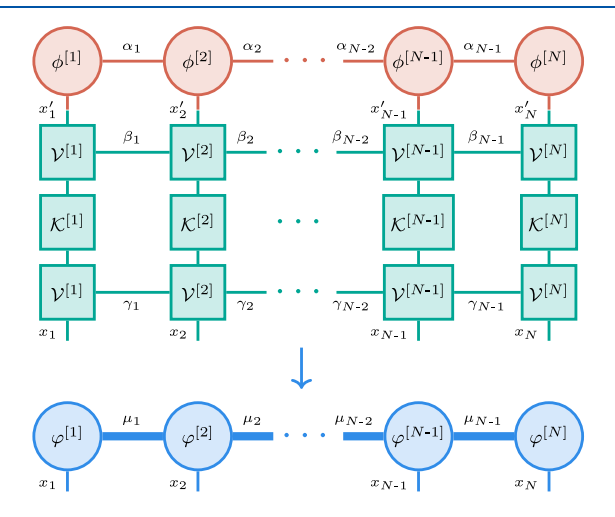


Figure 3. Figure shows the action of the time evolution operator onto the MPS wave function shown in eq 17. The one-dimensional unitary shown in Figure 2 is decomposed here into one-dimensional kinetic and potential propagators. Here, the initial vector is given by entanglement variables  $\overline{\alpha}$  while the Trotterized propagator in eq 17 has two entangled variables,  $\overline{\beta}$  and  $\overline{\gamma}$ , which combine to determine the index  $\overline{\mu} \equiv (\overline{\alpha}, \overline{\beta}, \overline{\gamma})$  for the propagated system.

Thus, given the "quantum-circuit-like" depiction in Figure 3, where the individual tensor cores may be interpreted as *qudit states*, this formalism allows a natural platform for constructing effective quantum algorithms.

Thus, now, the original multidimensional quantum propagation problem, has been partitioned into N one-dimensional independent subsystems. Each one corresponding to the terms in square brackets and defined as

$$\varphi_{\mu_{k-1}\mu_{k}}^{[k]x_{k}} \equiv \int dx_{k}' (\mathcal{V}_{\gamma_{k-1}\gamma_{k}}^{[k]x_{k}} \mathcal{K}_{x_{k}'}^{[k]x_{k}} \mathcal{V}_{\beta_{k-1}\beta_{k}}^{[k]x_{k}'}) \phi_{\alpha_{k-1}\alpha_{k}}^{[k]x_{k}'} 
= \int dx_{k}' \mathcal{U}_{\gamma_{k-1}\beta_{k-1}\gamma_{k}\beta_{k}}^{[k]x_{k}x_{k}'} \phi_{\alpha_{k-1}\alpha_{k}}^{[k]x_{k}'}$$
(18)

where the operators  $\{\mathcal{U}^{[k]}\}$  are denoted in Figure 2 and  $\{\mathcal{V}^{[k]}, \mathcal{K}^{[k]}\}$  in Figure 3 as green squares nodes. In some sense, the entanglement of the system is completely captured by these operations. Specifically, as laid out in Figure 3, the potential surface captures the entanglement within the system.

As a result, the action of the time-evolution operator on the initial MPS, is transformed into a set of parallel streams of one-dimensional effective quantum propagations. The use of parallel computational resources, both quantum and classical, comes together naturally, with a potential reduction in the total computational cost. In essence, the computational effort is now reduced:

$$O(D^N) \to O(ND |\overline{\mu}|_{\infty}^2)$$
 (19)

where  $|\overline{\mu}|_{\infty} \equiv \max\{\mu_k\}$ ,  $\forall k$ , is the  $L_{\infty}$ -norm of  $\overline{\mu}$ . It appears that we have eliminated the exponential scaling complexity of the dynamics on the left side and in fact the right-hand side has the appearance of a linear scaling complexity relation in N, which is certainly the case when  $\log_D |\overline{\mu}|_{\infty} \ll N$ . This aspect is also seen from the quantum circuit depiction of tensor network propagation discussion in Section III B.

III.A. Further Reduction in Complexity through the Use of Graph-Theoretic Electronic Structure. In a series of publications,  $^{60,170,171}$  we have shown that graph-theory based molecular fragmentation can be used to further reduce the complexity of the action of action of  $e^{-i\hat{V}\Delta t/2\hbar}$  on the initial MPS state. Specifically, when a molecular system  $^{173}$  is divided into a set of fragments treated as nodes in a graph, that are then connected based upon a distance cutoff criterion, to form edges, one obtains a graph-theory based molecular fragmentation approach where the energy function for a global potential surface becomes,

$$E_{\mathcal{R},\mathcal{G}}(\overline{\mathbf{x}}) = E^{\text{level},0}(\overline{\mathbf{x}}) + \sum_{r=0}^{\mathcal{R}} (-1)^r \sum_{\alpha \in \mathbf{V}_r} \Delta E_{\alpha,r}^{1,0}(\overline{\mathbf{x}}) \mathcal{M}_{\alpha,r}^{\mathcal{R}}$$
(20)

Here, the set of nodes is depicted as  $\mathbf{V}_0$ , the set of edges is depicted as  $\mathbf{V}_1$ , and the set of higher-order simplexes  $^{174-178}$  are denoted by the symbol  $\mathbf{V}_r$ . (Simplexes are defined as geometric objects with an arbitrary number of vertices, where all pairs of vertices are connected.) The above energy expression has been rigorously benchmarked for potential surfaces and AIMD over a set of publications  $^{60,90,91,170,171,173,179-188}$  and here  $E^{\text{level},0}(\overline{\mathbf{x}})$  is the energy at some lower-level of electronic structure theory, represented as *level*, 0, and this is corrected using graph-theoretically generated fragments,

$$\Delta E_{\alpha,r}^{1,0}(\overline{\mathbf{x}}) = E_{\alpha,r}^{\text{level},1}(\overline{\mathbf{x}}) - E_{\alpha,r}^{\text{level},0}(\overline{\mathbf{x}})$$
(21)

In eq 20,  $E_{\mathcal{R},\mathcal{G}}(\overline{\mathbf{x}})$  is the energy associated with molecular geometry  $\overline{\mathbf{x}}$  using graphical decomposition  $\mathcal{G}$ . This expression has been shown to serve well as an approximation to the energy at a higher level of electronic structure theory, level, 1. The quantity,  $\mathcal{R}$  is the rank of the largest simplex included, and captures the  $(\mathcal{R}+1)$ -body interaction terms between the nodal fragments.

As a result of the above, the action of  $e^{-i\hat{V}\Delta t/2\hbar}$  on the initial MPS state is simplified because the propagator,  $e^{-i\hat{V}\Delta t/2\hbar}$ , takes the following form in the coordinate representation when eq 20 is used to compute the potential surface:

$$\begin{split} \langle \overline{\mathbf{x}} | \exp\{-i\hat{V}t/2\hbar\} | \overline{\mathbf{x}} \rangle & \equiv \exp\{-iE_{\mathcal{R},\mathcal{G}}(\overline{\mathbf{x}})t/2\hbar\} \\ & = \exp{-i\left[E^{\text{level},0}(\overline{\mathbf{x}}) + \left\{\sum_{r=0}^{\mathcal{R}} (-1)^r \right. \right. \\ & \left. \sum_{\alpha \in \mathbf{V}_r} \Delta E_{\alpha,r}^{1,0}(\mathbf{R}_{\alpha,r}) \mathcal{M}_{\alpha,r}^{\mathcal{R}} \right\} t/2\hbar \\ & = \exp\{-i(E^{\text{level},0}(\overline{\mathbf{x}}) + \Delta E_{\mathcal{G}}(\{\overline{\mathbf{x}}\}))t/2\hbar\} \\ & = \exp\{-iE^{\text{level},0}(\overline{\mathbf{x}})t/2\hbar\} \exp\{-i\Delta E_{\mathcal{G}}(\{\overline{\mathbf{x}}\})t/2\hbar\} \end{split}$$

$$(22)$$

and

$$\begin{split} \exp\{-i\Delta E_{\mathcal{G}}(\{\overline{\mathbf{x}}\})t/2\hbar\} \\ &= \prod_{r=0}^{\mathcal{R}} \prod_{\alpha \in \mathbf{V}_r} \exp\{-i\{\Delta \tilde{E}_{\alpha,r}^{1,0}(\overline{\mathbf{x}})\}t \\ &\quad /2\hbar\} \\ &= \prod_{\alpha \in \mathbf{V}_0} \exp\{-i\Delta \tilde{E}_{\alpha,r=0}^{1,0}(\overline{\mathbf{x}}) \ t/2\hbar\} \\ &\prod_{\alpha \in \mathbf{V}_l} \exp\{-i\Delta \tilde{E}_{\alpha,r=1}^{1,0}(\overline{\mathbf{x}}) \ t/2\hbar\} \\ &\dots \\ &\prod_{\alpha \in \mathbf{V}_{\mathcal{R}}} \exp\{-i\Delta \tilde{E}_{\alpha,r=2}^{1,0}(\overline{\mathbf{x}}) \ t/2\hbar\} \end{split}$$

and

$$\Delta \tilde{E}_{\alpha,r}^{1,0}(\mathbf{R}_{\alpha,r}) = (-1)^r \Delta E_{\alpha,r}^{1,0}(\mathbf{R}_{\alpha,r}) \mathcal{M}_{\alpha,r}^{\mathcal{R}}$$
(24)

which is pictorially represented in Figure 4 for a rank-4 tensor. In Figure 4(a) we reproduce the action of the potential propagator on the initial wavepacket. The potential propagator is a rank-8 tensor written as an MPO. This is then readily approximated using lower rank tensors eq 22 in Figure 4(b) where, for simplicity, we only provide the  $\exp\{-i \Delta E_{\mathcal{G}}(\{\overline{\mathbf{x}}\})t/2\hbar\}$  portion of the propagator up to rank  $\mathcal{R}=1$ , that is only edges in the graph. We further make the notational simplification in the figure that,

$$\mathcal{V}_0^{[\alpha]} = \exp\{-i \Delta \tilde{E}_{\alpha,r=0}^{1,0}(\overline{\mathbf{x}}) t/2\hbar\}$$
 (25)

where the  $\alpha$ -th node propagator is a 2D tensor, or a 1D MPO. Similarly,

$$\mathcal{V}_{1}^{[\alpha_{1},\alpha_{2}]} = \exp\{-\iota \Delta \tilde{E}_{\alpha,r=1}^{1,0}(\overline{\mathbf{x}}) \ t/2\hbar\}$$
 (26)

where the  $\alpha$ -th edge is made of two nodes and depicted as  $[\alpha_1, \alpha_2]$ . The most important message from Figure 4 is that while 4(a) will necessitate the creation of an extended chain MPO propagator, given the potential surfaces from electronic structure are generally highly correlated, Figure 4(b) allows for an approximation, where at the most the MPOs may be rank-2, or some other lower rank tensor. In this manner, the use of graph-theoretic fragmentation brings down the

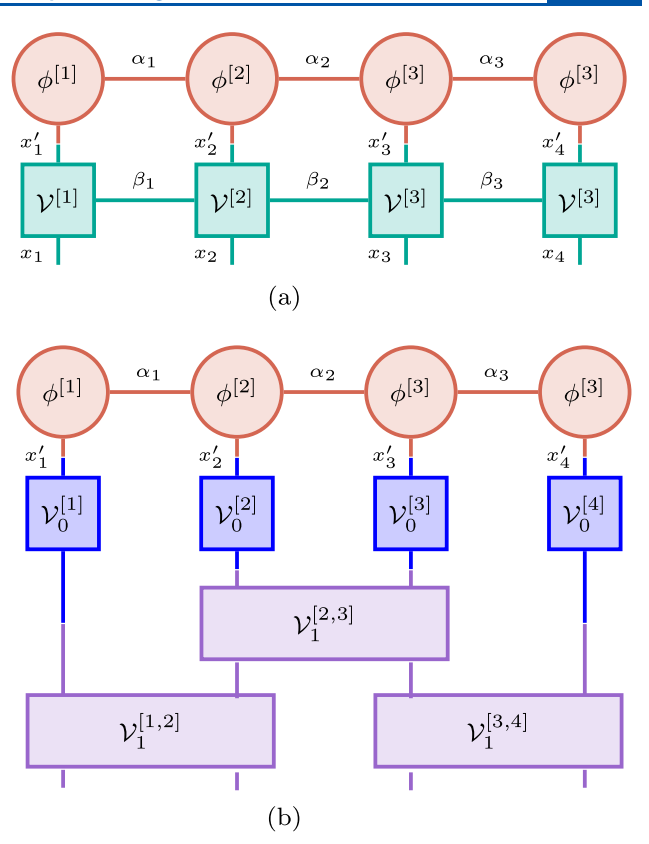


**Figure 4.** An illustration of the action of the graph theoretic potential propagator in eq 23 is shown in Figure (b), whereas Figure (a) shows the standard action of a correlated potential surface from electronic structure.

complexity of tensor network propagation. The full utility of the above expressions will be explored in detail in future publications.

**III.B. Quantum Circuit Representations for Tensor Network Propagation.** The algorithm above has a natural quantum-classical depiction in that the action of each reduced tensor core may be constructed on a set of distributed quantum platforms. A proof of concept quantum implementation of this idea has been tested on IonQ's ion-trap systems and paper is currently being prepared for publication. Given this quantum-classical flavor, we will also discuss here quantum circuit representations for the tensor network propagation scheme in eq 6. Our discussion is complemented by Figures 5 to 7. In Figures 5 and 6,  $|q_0\rangle$  and  $|q_1\rangle$  represent two different quantum degrees of freedom. These quantum degrees of freedom may themselves contain multiple qubits and this aspect is tersely assumed here. The precise number of qubits for each dimension depends on the number of basis functions,

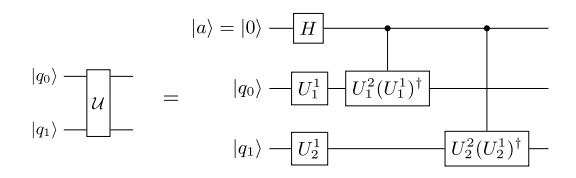


**Figure 5.** A quantum circuit for two dimensions, entangled in two internal dimensions,  $\mathcal{U} = \sum_{i=1}^2 U_1^i U_2^i$ . The complexity of each unitary is reduced through the tensor network formalism where each unitary now acts only on one dimension.

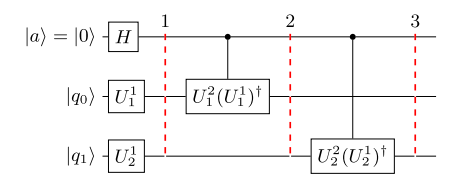


**Figure 6.** Same as Figure 5 but with individual steps emphasized and complemented by eqs 27 to 29.

or grid points, needed to represented each degree of freedom. In Figures 5 and 6, the ket- $|a\rangle$  represents a set of ancilla, and the entanglement between the  $\{|q_i\rangle\}$  degrees of freedom is controlled by the unitary operation  $\mathcal{U}=\Sigma_{i=1}^2U_1^iU_2^i$ . Note that having two terms in the summation allows for entanglement between  $|q_0\rangle$  and  $|q_1\rangle$ , and is a special case of eq 6. In the circuit shown in Figure 5,  $q_k$  is first transformed by  $U_k^1$ . After the Hadamard gate, the ancilla  $|a\rangle$  is in the superposition  $(|0\rangle+|1\rangle)/\sqrt{2}$  which splits the state in two parts. The state of the system is referred to as Stage 1 in Figure 6 and is given by

$$\textbf{Stage 1:} \frac{1}{\sqrt{2}} (|0\rangle + |1\rangle) \otimes U_1^{\text{l}} |q_0\rangle \otimes U_2^{\text{l}} |q_1\rangle \tag{27}$$

In Stages 2 and 3, in one part, corresponding to when the ancilla is  $|0\rangle$ , that is,  $(|0\rangle) \otimes U_1^{\rm l}|q_0\rangle \otimes U_2^{\rm l}|q_1\rangle$ ,  $q_k$  remains transformed by  $U_k^{\rm l}$ ; in the second part, that is,  $(|1\rangle) \otimes U_1^{\rm l}|q_0\rangle \otimes U_2^{\rm l}|q_1\rangle \text{ corresponding to when the ancilla is}$   $|1\rangle$ ,  $q_k$  becomes transformed by  $U_k^{\rm l}$ . Hence,

$$\begin{aligned} \textbf{Stage 2:} \quad & \frac{1}{\sqrt{2}} |0\rangle \otimes U_1^1 |q_0\rangle \otimes U_2^1 |q_1\rangle \\ & + \frac{1}{\sqrt{2}} |1\rangle \otimes [U_1^2 (U_1^1)^{\dagger}] U_1^1 |q_0\rangle \otimes U_2^1 |q_1\rangle \\ & = \frac{1}{\sqrt{2}} |0\rangle \otimes U_1^1 |q_0\rangle \otimes U_2^1 |q_1\rangle \\ & + \frac{1}{\sqrt{2}} |1\rangle \otimes U_1^2 |q_0\rangle \otimes U_2^1 |q_1\rangle \end{aligned} \tag{28}$$

and similarly

$$\begin{aligned} \textbf{Stage 3:} \quad & \frac{1}{\sqrt{2}} |0\rangle \otimes U_1^1 |q_0\rangle \otimes U_2^1 |q_1\rangle \\ & + \frac{1}{\sqrt{2}} |1\rangle \otimes U_1^2 |q_0\rangle \otimes [U_2^2 (U_2^1)^\dagger] U_2^1 |q_1\rangle \\ & = \frac{1}{\sqrt{2}} |0\rangle \otimes U_1^1 |q_0\rangle \otimes U_2^1 |q_1\rangle \\ & + \frac{1}{\sqrt{2}} |1\rangle \otimes U_1^2 |q_0\rangle \otimes U_2^2 |q_1\rangle \end{aligned} \tag{29}$$

and finally a measurement of the ancilla leads to the result

$$\frac{1}{2} \langle q_0 | U_1^{1\dagger} U_1^{1} | q_0 \rangle \langle q_1 | U_2^{1\dagger} U_2^{1} | q_1 \rangle \tag{30}$$

when the ancilla is in state  $|0\rangle$ , and

$$\frac{1}{2}\langle q_0^{}|U_1^{2\dagger}U_1^2|q_0^{}\rangle\langle q_1^{}|U_2^{2\dagger}U_2^2|q_1^{}\rangle \tag{31}$$

when the ancilla is in state |1⟩. That is the individual components of the propagated tensor network are found as outcomes based on the observation of the ancilla. The circuit therefore encodes the ability for one degree of freedom to become entangled with and drive evolution in the other. Additionally, the operators  $\{U_j^i\}$  are, as we will see later, all banded-Toeplitz matrices, when the kinetic energy part of the one-dimensional Hamiltonian is written using "Distributed Approximating Functionals (DAFs)".  $^{13,190-192}$ 

The final state at the end of the circuit depicted in Figure 7 is

$$\begin{split} &\frac{1}{2}|00\rangle\otimes\,U_1^1|q_0\rangle\otimes\,U_2^1|q_1\rangle\,+\,\frac{1}{2}|10\rangle\otimes\,U_1^2|q_0\rangle\otimes\,U_2^2|q_1\rangle\,+\\ &\frac{1}{2}|01\rangle\otimes\,U_1^3|q_0\rangle\otimes\,U_2^3|q_1\rangle\,+\,\frac{1}{2}|11\rangle\otimes\,U_1^4|q_0\rangle\otimes\,U_2^4|q_1\rangle \end{split} \tag{32}$$

and again, as in eqs 30 and 31, the respective components of the tensor network are measured outcomes from the ancilla. (The detailed development of eq 32 is given in Appendix A.)

In Figure 7, the circuit block between barriers 1 and 2 are  $C-U_f$  circuit blocks. These entangle the ancilla with the system. The last two gate operations, beyond barrier 2, entangle three or more sets of dimensions (and multiple qubits therein), through  $C-C-U_f$  circuit blocks, that will need careful handling and such gates generally yield greater error during computation. But, all unitary operations remain simplified in terms of the size of space these act upon, and this process can be generalized for arbitrary entanglement and for arbitrary number of quantum degrees of freedom.

For *N* dimensions, the circuit performs the operation

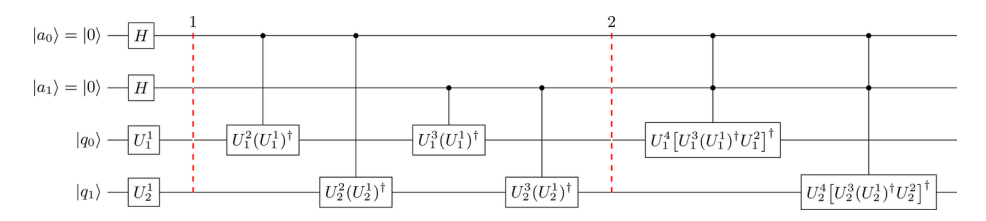


Figure 7. Similar to Figure 5, but now with four entanglement dimensions,  $\mathcal{U} = \sum_{i=1}^{4} U_1^i U_2^i$ . Clearly the complexity grows with greater entanglement.

$$\sum_{i} |i\rangle_{\!a} \otimes U_1^i |q_0\rangle \otimes U_2^i |q_1\rangle \otimes \cdots \otimes U_N^i |q_{N-1}\rangle \tag{33}$$

Here we have chosen to use the integer representation for the ancilla qubits and depict these as  $|i\rangle_a$ . Additionally, there is inherently a map between this integer index and the entanglement index  $\overline{\beta}$  in eq 5. That is,

$$\overline{\beta} \rightarrow |i\rangle_a$$
 (34)

Hence, between eqs 5 and 33

$$\mathcal{U}_{\beta_1}^{[1]} \to U_1^i$$
 (35a)

$$\mathcal{U}^{[j]}_{\beta_{j-1}\beta_{j}} \to U^{i}_{j}$$
 (35b)

$$\mathcal{U}_{\beta_{N,1}}^{[N]} \to U_N^i$$
 (35c)

Proceeding along the directions laid out in Figure 7, this will need  $[C-U_f]$ ,  $[C-C-U_f]$ ,  $[C-C-W_f]$  circuit blocks that are extremely difficult to implement on current quantum hardware and lead to enormous error. <sup>192</sup>

As the entanglement increases, the number of ancilla required increases in a logarithmic fashion (number of ancilla is the base-2 log of the extent of entanglement), and the complexity of the circuit, in terms of the necessary number of entanglement gates, also increases. One way to reduce the number of such control gates can be achieved by using as many more ancilla-qubits as the number of terms in the summation, that is the extent of entanglement. This may eliminate the need for the higher order entanglement gates  $[C-C-U_f]$ ,  $[C-C-\cdots-C-U_f]$ , etc., but may increase need for more quantum resources.

It is however crucial to note the exponential scaling of full quantum propagation with nuclear dimensions, as emphasized in earlier sections has already been alleviated to a large extent through the circuits above. For a system with N nuclear dimensions with D discretizations per dimension, the state vector's size grows as  $D^N$ , leading to a unitary operator size of  $D^{2N}$  that is required to propagate such a state. However, leveraging Tensor Network techniques, as emphasized in eq 19, each unitary operator's size in Figure 7 is  $D^2$ , suggesting a mitigation of the exponential scaling with nuclear dimensions. Nonetheless, the number of such unitaries would grow as the extent of entanglement, and this is indicated by the factor  $N|\overline{\mu}|_{\infty}^2$  introduced in eq 19. Consequently, as the entanglement dimensions increase, the parameter  $|\overline{\mu}|_{\infty}$  grows, hence, the circuit gets more complicated as can be seen from Figure 7.

In a manuscript currently under preparation, <sup>189</sup> we alleviate this problem by constructing a quantum classical scheme, and in future publications we will discuss new strategies that combine this approach with the natural tensor network form of the potential propagator that arises as a result of use of a graph-theoretically generated molecular fragmentation as discussed above. <sup>60</sup>

# IV. THE EXPONENTIAL GROWTH OF THE BOND DIMENSIONS IN EQ 17

It is critical to analyze the term  $\overline{\mu}$ , on the right side of eq 19. In fact, as already seen before <sup>50</sup> (and in Figures 2, 5 and 7), this term grows exponentially with time and affects the complexity. In fact, after  $N_t$  time-steps, i.e.  $N_t$  actions of eq 16,

$$|\overline{\mu}|_{\infty} \to |\overline{\alpha}|_{\infty} \{|\overline{\beta}|_{\infty}\}^{2N_t}$$
 (36)

where  $|\overline{\alpha}|_{\infty}$  and  $\{|\overline{\beta}\>|_{\infty}\}$  are the  $L_{\infty}$ -norms of the entanglement variables in eqs 3 and 12. The parameters  $|\overline{\alpha}\>|_{\infty}$  and  $\{|\overline{\beta}\>|_{\infty}\}$  here, also signifies the upper bound to the MPS and MPO bond-dimension, respectively. In the discrete position basis  $\{|\overline{\mathbf{x}}\>\rangle\}$ , these upper bounds correspond to the number of discretizations chosen along each dimension, or simply put, the number of grid points along each spatial dimension. Thus, the right side of eq 19, which appears to be devoid of the exponential scaling in N, gathers instead a potentially catastrophic scaling in time which complicates the quantum circuit description and is a serious problem as dynamical systems evolve in time. Indeed this aspect can be seen in Figure 8, which depicts how the

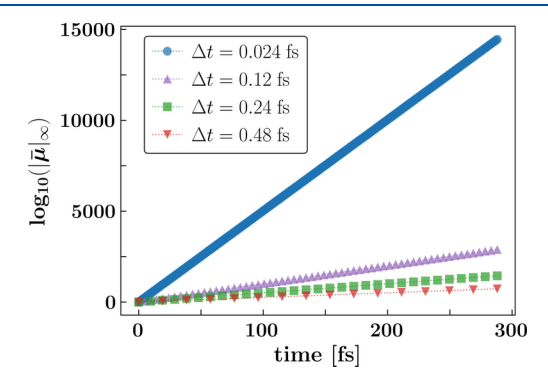


Figure 8. Exponential increase in  $|\overline{\mu}|_{\infty}$  (eq 36) as a function of time.

quantity  $|\overline{\mu}|_{\infty}$  would grow exponentially for a two-dimensional system, if propagated over time. However, it is important to note here that the bond-dimension growth is purely a numerical artifact which arise due to multiplication of bond indices and does not represent any physical growth in entanglement of the system. In Section IV A, we provide a variational algorithm to reduce this complexity in time.

One must also note the following key comments with respect to analysis in eqs 17 and 18. First, the number of entanglement variables involved in eq 13 has a key role in the efficiency of propagation scheme in eq 17. This is also seen from the discussion in Section III B. Second, as previously stated, the error in the Trotter approximation is governed by the time-step size  $\Delta t$ . In other words, the necessary precision in the quantum propagation of an arbitrary state, requires a sufficiently large number of steps  $N_t \equiv t/\Delta t$ . In the TN framework discussed above, a naive implementation of the time-evolution procedure involves the direct MPO-MPS multiplication at each time-step, resulting in a potentially exponential increase of the entanglement dimension  $\overline{\eta}$  (which now would be the maximum number of entanglement dimensions in  $\overline{\mu} = {\overline{\alpha}, \overline{\beta}, \overline{\gamma}}$ , represented as  $|\overline{\mu}|_{\infty}$  in eq 19 (see also eq 36 and Figure 8).

In order to shed some light into this matter, let us define  $\psi_{\nu}(\overline{\mathbf{x}}; t + \Delta t)$  as the "partially-evolved" wave function generated by the action of the potential sector of the time-evolution operator, eqs 11 and 12, on the initial wave function of eq 3. We may then write the result in MPS form as

#### Scheme 1

```
Algorithm 1 Regularization of the bond dimension (QR-SVD).
Require: N-2 order-3 tensors \phi^{[k]} (for k \in [2, N-1]) and order-2 tensors \phi^{[1]} and \phi^{[N]}, obtained from the MPS representation
          of the propagated wavefunction \psi_v(\bar{\mathbf{x}}; t + \Delta t)
          QR Decompositions
  \begin{array}{l} 1: \ \mathsf{QR}(\phi^{[1]}) \to Q^{[1]}, R^{[1]} \\ 2: \ \mathbf{for} \ k = 2, N-1 \ \mathbf{do} \\ 3: \qquad \phi^{[k]} = \mathtt{reshape}(\phi^{[k]}, (\eta'_{k-1}D_k), \eta'_k) \\ 4: \qquad \mathsf{QR}(\phi^{[k]}) \to Q^{[k]}, R^{[k]} \end{array}
                                                                                                                                                                  \triangleright QR decomposition of input \phi^{[1]} and output Q^{[1]},R^{[1]}
                                                                                                                                                      \qquad \qquad \triangleright \text{ Reshape order-3 tensor } \phi^{[k]} \text{ into matrix} \\ \triangleright \text{ QR decomposition of reshaped } \phi^{[k]} \text{ with outputs } Q^{[k]}, R^{[k]} \\
  5: end for 6: \mathbb{QR}(\phi^{[N]}) \to R^{T^{[N]}}, Q^{T^{[N]}}
                                                                                                                                                                                                      \triangleright Transpose QR decomposition of \phi^{[N]}
   \begin{array}{l} Singular\ Value\ Decompositions\\ 7:\ \mathbf{for}\ k=2,N-1\ \mathbf{do}\\ 8:\ \ Q^{[k]}=\mathbf{reshape}(Q^{[k]},\eta_k,D_kr_k^q)\\ 9:\ \ \ \mathrm{SVD}(R^{[k-1]}Q^{[k]},\varepsilon)\to U^{[k-1]},W^{[k-1]},\lambda^{[k-1]} \end{array} 
                                                                                                                                                    \triangleright Reshape Q^{[k]} from r_k^q \times r_k^q to \eta_k' \times (D_k r_k^q) (r_k^q \equiv \operatorname{rank} Q^{[k]})
                                                                                                                                                                                                  \triangleright Truncated SVD with \varepsilon error threshold
             U_i^{[k-1]j} = U_i^{[k-1]j} \sqrt{\lambda_i^{[k-1]}}
                                                                                                                                                                                       ▷ Re-scaling of left and right singular vectors
11: W_i^{[k-1]j} = W_i^{[k-1]j} \sqrt{\lambda_j^{[k-1]}}
12: end for 13: \ \mathrm{SVD}(R^{[N-1]}R^{T[N]},\varepsilon) \to U^{[N-1]},W^{[N-1]},\lambda^{[N-1]}
                                                                                                                                                                                                   > Singular vectors are re-scaled as above
\begin{array}{ll} Recovery\ of\ MPS\ structure \\ 14:\ \mathbf{for}\ k=2,N-1\ \mathbf{do} \\ 15: \qquad W^{[k-1]} = \mathbf{reshape}(W^{[k-1]},\Gamma_{k-1}D_k,r_k^q) \\ 16: \qquad \tilde{\phi}^{[k]} = W^{[k-1]}\times U^{[k]} \end{array}
17: end for
18: \tilde{\phi}^{[1]} = Q^{[1]} \times U^{[1]}
19: \tilde{\phi}^{[N]} = W^{[k-1]} \times Q^{T^{[N]}}
```

$$\psi_{\nu}(\overline{\mathbf{x}}; t + \Delta t) \equiv \langle \overline{\mathbf{x}} | e^{-i\hat{V}\Delta t/2\hbar} | \Psi(t) \rangle 
= e^{-iV(\overline{\mathbf{x}})\Delta t/2\hbar} \psi(\overline{\mathbf{x}}; t) 
= \sum_{\overline{\alpha}'} \phi_{\alpha_{1}'}^{\prime[1]x_{1}} \phi_{\alpha_{1}'\alpha_{2}'}^{\prime[2]x_{2}} \dots \phi_{\alpha_{N-2}'\alpha_{N-1}'}^{\prime[N-1]x_{N-1}} \phi_{\alpha_{N-1}'}^{\prime[N]x_{N}}$$
(37)

where

$$\phi_{\alpha_{1}^{'}}^{'[1]x_{1}} \equiv \mathcal{V}_{\beta_{1}}^{[1]x_{1}} \phi_{\alpha_{1}}^{[1]x_{1}} \tag{38a}$$

$$\phi_{\alpha'_{j-1}\alpha'_{j}}^{\ '[j]x_{j}} \equiv \mathcal{V}_{\beta_{j-1}\beta_{j}}^{[j]x_{j}} \phi_{\alpha_{j-1}\alpha_{j}}^{[j]x_{j}} \tag{38b}$$

$$\phi_{a'_{N-1}}^{\prime[N]x_N} \equiv \mathcal{V}_{\beta_{N-1}}^{[N]x_N} \phi_{a_{N-1}}^{[N]x_N}$$
(38c)

Notice the product on the right side of (eq 28b) is strictly speaking an order-5 tensor (order-3 for eqs 38a and 39c); however, in order to keep the MPS structure, each tensor may be reshaped via the index fusion  $\alpha_k \beta_k > \alpha_k'$ , such that the original double sum over  $\overline{\alpha}$  and  $\overline{\beta}$  is now spanned by the single sum over  $\overline{\alpha}'$ .

It should be stressed, however, that the enlarged entanglement dimensions  $\overline{\eta}'$ , now defined as the upper limits of  $\alpha'_k$ , no longer depict the actual physical entanglement of the evolved state, but rather it is merely an algebraic artifact of the MPO-MPS multiplication. This is best understood by first recalling that the order-2 and order-3 tensors in the MPS expansion, by construction, consist of left and right singular vectors arising from the sequence of SVD's between multiple bipartite subsystems. On the contrary, after the MPO-MPS multiplication yielding eq 37, the resulting MPS structure comes with a caveat: each tensor in the expansion is not comprised of singular vectors. The reason being that because the SVD is a rank-revealing factorization, <sup>193–195</sup> the number of actual singular vectors is bounded from above by the physical dimensions, namely, the total number of grid points per spatial dimension. On the other hand, the number of the resulting "pseudo-singular vectors" in eq 37, i.e., the updated bond dimension  $\overline{\eta}'$ , is unbounded and can grow exponentially with the number of time-steps  $N_t$ .

The true entanglement is naturally revealed by computing the von-Neumann entropy or any alternative entanglement measure, 196 so to avoid confusion we will address hereafter this "artificial entanglement" exclusively as bond dimension. Admittedly, the entanglement entropy could potentially increase as the state evolves in time; 50,197,198 however, its growth rate may be expected to be substantially lower than that of the bond dimension and is always determined by the "true" entanglement present in the potential as seen from Figure 3. The kinetic sector of the time-evolution operator defined in eq 14, which is conveniently factorizable into one-dimensional free propagators, clearly does not contribute to the bond dimension increase, since the  $\mathcal{K}_{x_k}^{x_k'}$  terms can be interpreted as the tensor cores of a trivial MPO, that is, with bond dimensions equal to one. Therefore, at second order in the Trotter-Suzuki approximation, eq 10, the bond dimension is increased quadratically per time-step, which is the reason for the "2" in the exponent in eq 36.

Additionally, when constructing fully *ab initio* potential surfaces, such as in previous studies <sup>170,171</sup> and also as described briefly in Section III A, the resulting potential may exhibit coupling across dimensions, unlike model-based or fitted potentials. Ab initio potentials, computed on-the-fly, do not naturally decompose into many-body interaction terms, posing challenges in writing the action of the potential propagator on a state with uncontrollable bond dimensions. However, in publication<sup>60</sup> and as described in Section III A, it has been demonstrated that graph-theory based molecular fragmentation methods provide a natural tensor network-type decomposition of the potential propagator. This approach offers advantages, including subkcal/mol accuracy in potential surfaces, especially when coupled cluster accuracy is required. In future publications we will combine the approach presented here with that in ref.<sup>60</sup> toward a fully ab initio treatment of quantum nuclear dynamics using tensor networks on both quantum and classical hardware architectures, with on-the-fly

IV.A. A Regularization Algorithm to Control the Exponential Increase in Bond Dimension. It is clear from the above discussion, that the regularization of the bond dimension is a crucial measure for controlled quantum propagation of tensor networks. If this issue is not handled

properly, the storage complexity at multiple time-step calculations becomes rapidly unmanageable. Furthermore, as seen in Section III B, the quantum circuit complexity increases with entanglement. A truncation scheme that prevents the loss of computational tractability is, therefore, undoubtedly necessary.

Thus, we now introduce an algorithm aimed to regularize the bond dimension of the MPS representation of wave functions along its time-evolution. This is a key step in our algorithm and critical differences from other methods 135,199 are noted in Supporting Information.

The key objective of the following methodology is to minimize the subspace spanned by the updated pseudosingular vectors. We do this by exploiting a gauge invariance embedded within each bond dimensional subspace. This allows us to transform each individual stream independently to find the minimal subspace basis that may correspond to the singular vectors of the updated MPS. The result is a chain of orthogonal matrices whose columns span the minimal orthogonal subspace of smaller size than the updated bond dimensions  $\overline{\eta}'$ .

The bond dimension regularization algorithm has three steps that are described in the paragraphs below. These are also succinctly outlined in Algorithm 1 in Scheme 1.

IV.A.1. Rank Determination of  $\{\phi_{\alpha_{k-1}'\alpha_{k}'}^{\prime[k]x_{k}}\}$  from Eq 38a through QR Decomposition. As in ref 199., we begin by rotating the column and row vectors of each tensor core  $\phi'^{[k]}$ in the updated wave function eq 37, by means of QR decomposition of each one of these tensors. The QR factorization of the first and last tensors, being of order-2, are straightforward and shown in eqs 39a and 39c. Notice, however, that the  $N^{th}$  tensor has the transpose shape of the first, and so its actual decomposition is rather of the form  $R^{T}Q$ . On the other hand, the order-3 tensors must be reshaped into order-2 tensors (first row of Figure 9) prior to the QR

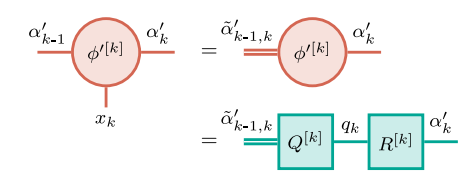


Figure 9. QR decomposition of order-3 tensors. The index fusion  $\alpha'_{k-1}x_k > \tilde{\alpha}'_{k-1,k}$ , depicted as double-line edges, reshapes the order-3 tensor  $\phi'^{[k]i_k}_{a'_{k-1}a'_k}$  into a reduced order tensor  $\phi'^{[k]\tilde{a}'_{k-1,k}a'_k}$ , i.e., a matrix which is then factorized via QR decomposition.

decomposition (green boxes in Figure 9); this is achieved by combining the physical index  $x_k$  with the left bond index  $\alpha'_{k-1}$ , namely, with the index fusion  $\alpha'_{k-1}x_k \succ \tilde{\alpha}'_{k-1,k}$ . These operations are succinctly summarized in the following equations:

$$\phi_{\alpha'_{1}}^{'[1]x_{1}} = \sum_{q_{1}} Q_{q_{1}}^{[1]x_{1}} R_{\alpha'_{1}}^{[1]q_{1}}$$

$$\phi_{\alpha'_{k-1}\alpha'_{k}}^{'[k]x_{k}} \xrightarrow{\alpha'_{k-1}x_{k} > \tilde{\alpha}'_{k-1,k}} \phi_{\alpha'_{k}}^{'[k]\tilde{\alpha}'_{k-1,k}}$$

$$\phi_{\alpha'_{k}}^{'[k]\tilde{\alpha}'_{k-1,k}} = \sum_{q_{k}} Q_{q_{k}}^{[k]\tilde{\alpha}'_{k-1,k}} R_{\alpha'_{k}}^{[k]q_{k}}$$
(39a)

$$\phi_{\alpha'_{k}}^{'[k]\tilde{\alpha}'_{k-1,k}} = \sum_{q_{k}} Q_{q_{k}}^{[k]\tilde{\alpha}'_{k-1,k}} R_{\alpha'_{k}}^{[k]q_{k}}$$
(39b)

$$\phi_{\alpha'_{N-1}}^{'[N]x_N} = \sum_{q_N} R^T_{\alpha'_{N-1}}^{[N]q_N} Q^T_{q_N}^{[N]x_N}$$
(39c)

where  $Q^{[k]}$  and  $R^{[k]}$  are unitary and upper triangular matrices, respectively. The diagrammatic representation of these two operations is depicted in Figure 9.

Notice the reshaping direction is arbitrary and can be equally chosen in the opposite direction, i.e.,  $\alpha'_k x_k > \tilde{\alpha}'_{k,k}$ . This arbitrariness is not dissimilar to the method of construction of tensor networks,<sup>23</sup> where a chosen network graph, along with a chosen direction of processing affects the extent of perceived entanglement. In our case, the goal is to reduce the degree of arbitrariness as seen from the so-called "artificial entanglement vectors" above and hence the particular choice of direction here is not essential.

IV.A.2. Gauging Entanglement across Neighboring Reduced Rank Tensor Cores through Sequential SVD Steps. This stage, as we discuss below, involves a critical difference between our approach and other methods, 199 to reduce the size of the entanglement dimensions. In this stage, the resulting tensor cores from the previous step are grouped and reshaped such that the product between neighboring QRfactorization pairs  $R^{[k-1]}Q^{[k]}$  (l.h.s. of Figure 10) is defined by

Figure 10. SVD of adjacent RQ matrices. The reshape operation on  $Q^{[k]}$  via the index split  $\tilde{\alpha}'_{k-1,k} \prec \alpha'_{k-1}x_k$  followed by  $x_kq_k \succ \tilde{q}_{k,k}$ , defines the matrix product as the index contraction over  $\alpha'_{k-1}$ . The product  $R^{[k-1]}Q^{[k]}$  is then factorized via SVD.

contracting the bond index  $\alpha'_k$ , which is the original entanglement index in eq 37. This is shown on the first row, r.h.s., of Figure 10. To achieve these steps, the previously reshaped index  $\tilde{\alpha}'_{k-1,k}$  of  $Q^{[k]}$ , must be split as  $\tilde{\alpha}'_{k-1,k} \prec \alpha'_{k-1}x_k$ and then fuse the physical index  $x_k$  with the QR-index  $q_k$ , as  $x_k q_k > \tilde{q}_{k,k}$ . The order-2 tensor resulting from the  $\alpha'_{k-1}$  index contraction of  $R^{[k-1]}Q^{[k]}$ , is then decomposed via a truncated SVD (second row of Figure 10), which discards the smallest singular values according to an assigned tolerance parameter  $\varepsilon$ .

The different tensor cores are thus transformed as

$$Q_{q_{k}}^{[k]\tilde{\alpha}'_{k-1,k}} \xrightarrow{\tilde{\alpha}'_{k-1,k} \prec \alpha'_{k-1}x_{k}} Q_{\tilde{q}_{k,k}}^{[k]\alpha'_{k-1}}$$

$$\sum_{\alpha'_{k-1}} R_{\alpha'_{k-1}}^{[k-1]q_{k-1}} Q_{\tilde{q}_{k,k}}^{[k]\alpha'_{k-1}} = \sum_{\sigma_{k-1}=1}^{\Gamma_{k-1}} U_{\sigma_{k-1}}^{[k-1]q_{k-1}} W_{\tilde{q}_{k,k}}^{[k-1]\sigma_{k-1}}$$

$$(40a)$$

$$R_{\alpha'_{N-1}}^{[N-1]q_{N-1}}R^{T}_{\alpha'_{N-1}}^{[N]q_{N}} = \sum_{\sigma_{N-1}=1}^{\Gamma_{N-1}} U_{\sigma_{N-1}}^{[N-1]q_{N-1}}W_{q_{N}}^{[N-1]\sigma_{N-1}}$$
(40b)

The tensor cores  $U^{[k]}$  and  $W^{[k]}$ , which are the left and rightorthogonal matrices from the SVDs, contain the left and right singular vectors, respectively, and are also rescaled by its singular values, as it was done in eqs 4a to 4c. The total number of singular values retained in the  $k^{\text{th}}$  SVD is denoted

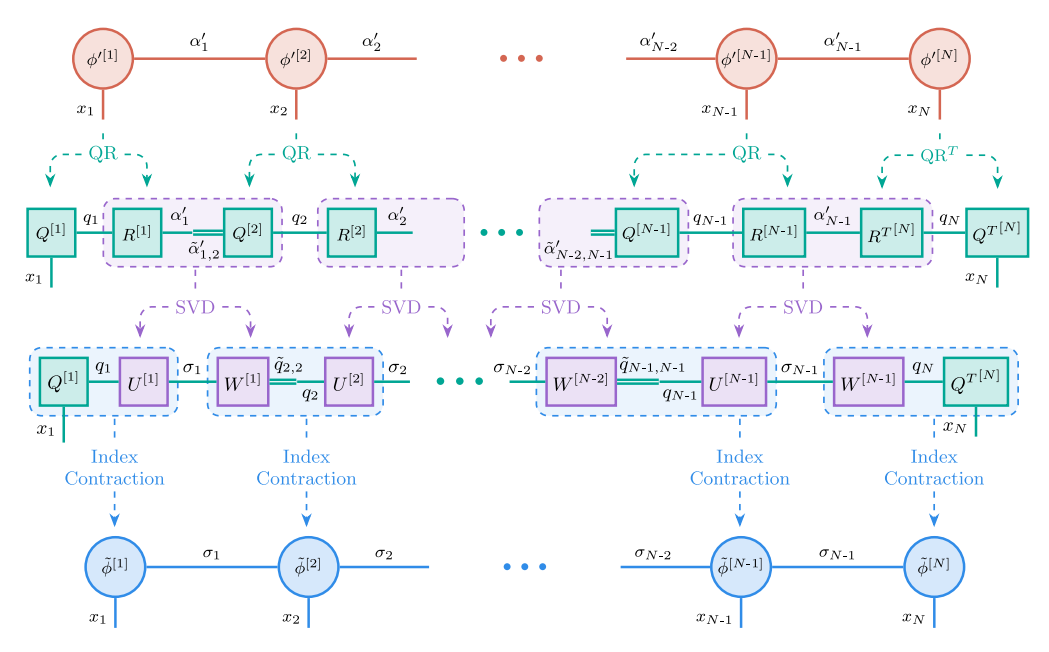


Figure 11. QR-SVD Regularization. The Matrix Product State (MPS) representation of the time-evolved wave function  $\psi(\overline{\mathbf{x}}; t + \Delta t)$ . The middle rank-3 tensors  $\phi_{\alpha'_1\alpha'_2}^{\prime [2]x_2}$  and  $\phi_{\alpha'_2\alpha'_3}^{\prime [3]x_3}$  are first reshaped by the index fusions  $\alpha'_1x_2 > \tilde{\alpha}'_{1,2}$  and  $\alpha'_2x_3 > \tilde{\alpha}'_{2,3}$ , respectively. A QR decomposition of each of the  $\phi'^{[k]}$  tensors is applied, followed by an SVD of the product of the tensors enclosed by the purple-dashed square.

by  $\Gamma_k$ . The wave function, whose TN-diagram is shown on the third row of Figure 11, is thus written as

$$\begin{split} \psi_{\nu}(\overline{\mathbf{x}};\,t+\Delta t) &= \sum_{\overline{\mathbf{q}}} \sum_{\overline{\sigma}}^{\overline{\Gamma}} Q_{q_{1}}^{\,[1]x_{1}} U_{\sigma_{1}}^{\,[1]q_{1}} W_{\bar{q}_{2,2}}^{\,[1]\sigma_{1}} \dots \\ &\times \dots U_{\sigma_{j-1}}^{\,[j-1]q_{j-1}} W_{\bar{q}_{j,j}}^{\,[j-1]\sigma_{j-1}} \dots \\ &\times \dots U_{\sigma_{N-1}}^{\,[N-1]q_{N-1}} W_{q_{N}}^{\,[N-1]\sigma_{N-1}} Q_{q_{N}}^{\,T\,\,[N]x_{N}} \end{split} \tag{41}$$

The step above is critical in our algorithm. It differs from other methods in the following ways. First, we reiterate that the goal of the algorithm is to find the "true" bond dimension in a MPS. Ideally, one could achieve this by essentially reconstructing the whole MPS by doing a sequence of N-1 SVDs between each pair of tensor nodes, analogous to the standard MPS construction. As noted in ref 199., these are indeed computationally challenging since these matrices grow in size with dimension. To overcome this issue, the proposed solution in ref 199. consisted of an algorithm that similarly involves a series of QR and SVD factorizations, which must be performed in sequential order (see Supporting Information for a concise explanation of the algorithm). In our case, the computational burden of the rank reduction is greatly alleviated by only considering the neighboring tensor cores, as outlined in Figure 11, allowing the parallel construction our SVD bases vectors.

Therefore, by tracing over the  $\{\alpha_j'\}$  indices in eq 40a and then following that with the SVD step in eq 40b, we have essentially followed the same recipe of the "ideal" sequence of SVDs, albeit in a numerically efficient fashion. We have thus arrived at the new family of compressed entanglement indices:  $\overline{\alpha}' \to \overline{\sigma}$  with regularized bond dimensions  $\overline{\Gamma}$ .

IV.A.3. Creating the Final MPS State Vectors through Intermediate Index Contraction. At this stage, it is critical to take note of the penultimate row in Figure 11. The sequence of

SVD steps above have provided us with the new bond indices,  $\overline{\sigma}$ . These will become central to our MPS state. However, the left and right singular vectors can be separately contracted to their neighboring counterparts as indicated through dashed rectangles in the penultimate row of Figure 11, which require a prior reshape via the index split  $\tilde{q}_{k,k} \prec x_k q_k$ . The index contraction operation are therefore carried out as follows

$$\sum_{q_1} Q_{q_1}^{[1]x_1} U_{\sigma_1}^{[1]q_1} = \tilde{\phi}_{\sigma_1}^{[1]x_1} \tag{42a}$$

$$W_{\tilde{q}_{k,k}}^{[k-1]\sigma_{k-1}} \xrightarrow{\tilde{q}_{k,k} \prec x_k q_k} W_{\sigma_{k-1}}^{[k-1]x_k q_k}$$

$$\sum_{q_k} W_{\sigma_{k-1}}^{[k-1]x_k q_k} U_{\sigma_k}^{[k]q_k} = \tilde{\phi}_{\sigma_{k-1}\sigma_k}^{[k]x_k}$$
(42b)

$$\sum_{q_{N}} W_{\sigma_{N-1}}^{[N-1]q_{N}} Q^{T}_{q_{N}}^{[N]x_{N}} = \tilde{\phi}_{\sigma_{N-1}}^{[N]x_{N}}$$
(42c)

Hence, the evolved state is finally returned into an MPS structure by contracting the QR index  $q_k$ , which leaves behind the real space index  $x_k$  during every such trace. The partially updated wave function thus takes the familiar form

$$\psi_{\nu}(\overline{\mathbf{x}}; t + \Delta t) = \sum_{\bar{\sigma}}^{\bar{\Gamma}} \tilde{\phi}_{\sigma_{1}}^{[1]x_{1}} \tilde{\phi}_{\sigma_{1}\sigma_{2}}^{[2]x_{2}} \dots \tilde{\phi}_{\sigma_{N-2}\sigma_{N-1}}^{[N-1]x_{N-1}} \tilde{\phi}_{\sigma_{N-1}}^{[N]x_{N}}$$
(43)

which is analogous to eq 37 but with the resulting MPS bond indices being the now regularized  $\overline{\sigma} = {\sigma_1, ..., \sigma_{N-1}}$ .

In this fashion, we perform an efficient Schmidt-like decomposition, potentially every few steps in our quantum propagation, to compress and probe the degree of accumulated entanglement during dynamics.

To conclude this section we reiterate, as depicted in Figures 11 and 12, that our approach involves a sequence of QR decompositions and SVDs that act in parallel on individual

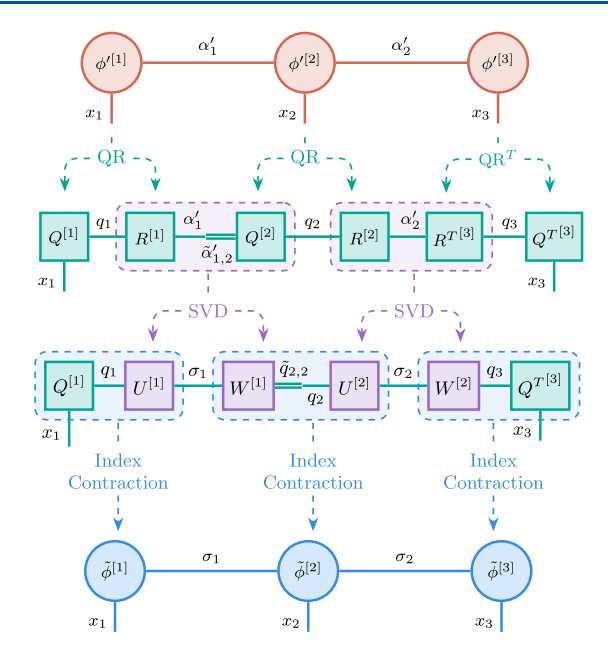


Figure 12. Diagram above illustrates the process outlined in Figure 11 for the case of three quantum nuclear dimensions. Each tensor  $\phi^{r[k]}$  undergoes a QR decomposition, followed by a singular value decomposition (SVD) of the resulting product tensors.

cores and on entanglement variables that couple neighboring cores. This aspect is especially critical as discussed in Supporting Information.

Discussing briefly the accuracy of the method, which is elaborated upon in detail in Section V B and in Supporting Information, we note our simulation begins with a left canonical MPS initial wavepacket. Subsequently, we exclusively utilize unitary operations to propagate the MPS initial wavepacket. Hence, the error in the propagated MPS primarily arises from truncation via the chosen singular value threshold, as outlined in the Supporting Information, during a sequence of QR decompositions and SVDs applied to the individual cores of the MPS. Additionally, another source of error affecting the full quantum propagation of the nuclear wave function is the error resulting from the trotter approximation of the unitary propagator, as depicted in eq 10.

Furthermore, given that both QR-decomposition and SVD are composed from unitary transforms that employ Householder, Givens, and Jacobi primitive operations, 193 it may be possible to implement the QR-decomposition and SVD steps using quantum algorithms in future. For instance, the SVD for any matrix A can be equivalently approached as the eigenvalue problem for  $A^{T}A$  and  $AA^{T}$ , which can be mapped to two parallel quantum algorithms. Furthermore, the algorithm discussed in this study exclusively considers immediate pairs, implying that the size of the matrix A would be on the order of the number of discretizations for each dimension. Thus, it is conceivable that a phase estimation algorithm applied to a problem of the order of a 1D system could yield the SVD. Integration of these quantum algorithms would transition a significant portion of the operations described in Figure 11 to quantum operations, thereby enhancing the computational capability of this approach. However, a critical challenge in such quantum algorithms would be the elimination of numerically insignificant singular values, as indicated in steps two and three of Figure 11. If this step could be performed using some kind of a quantum annealing step,200 that would

facilitate the translation of the algorithm to a full quantum process.

In the next section, we will show how this algorithm is applied to the correlated time-evolution of the nuclear degrees of freedom in a symmetric hydrogen-bonded system.

# V. QUANTUM DYNAMICS IN A SHORT-STRONG, SYMMETRIC HYDROGEN-BONDED SYSTEM

Short-strong hydrogen bonds<sup>201-203</sup> are abundant in biological, materials, and atmospheric systems and are characterized by the often highly anharmonic nature of the potential energy surfaces (PES)<sup>204–211</sup> that confine the hydrogen nuclear degrees of freedom. For example, it is well-known<sup>211</sup> that such confining potentials can be at least quartic, and sometimes sixth order or higher. Thus, the commonly used harmonic approximation is inadequate to address such chemical dynamics problems. Such fluctuations are normally referred to as gating modes in hydrogen transfer reactions.<sup>212</sup> Furthermore, the anharmonic potential fluctuates and changes its shape with the donor-acceptor distance. Therefore, a full quantum dynamical simulation is often required to accurately predict the chemical properties of such complex systems, 211,213,214 as these involve the correlated interplay between multiple nuclear degrees of freedom.

To probe and illustrate the accuracy and efficiency of the TN method introduced in the previous section, we consider the symmetric short-strong hydrogen-bonded system within the bidentate-chelating agent, 2,2'-bipyridine. The aromatic nitrogen-containing heterocycles within this molecule are of significance in numerous applications in energy storage and catalytic oxidation. The protonated 2,2'-bipyridine molecule has been widely studied due to its potential applications as electron carriers and electron acceptors, whereas the deprotonated form is a strong chelating agent. As shown in Figure 13, the system contains a

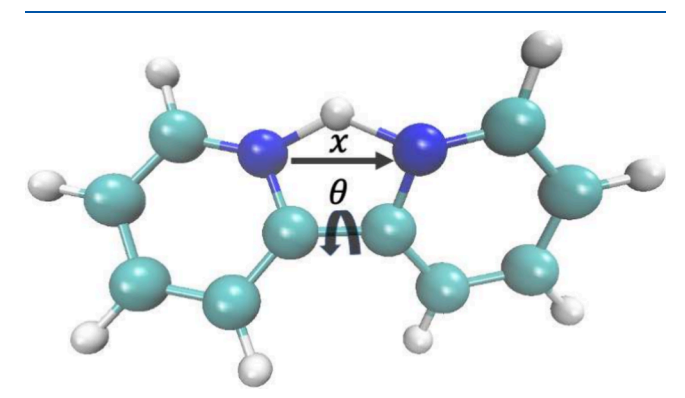


**Figure 13.** Protonated 2,2'-bipyridine molecule. The shared proton is shown in a symmetric position between the donor and acceptor nitrogen atoms at the transition state geometry. The two degrees of freedom defining the PES,  $\{x,\theta\}$ , are also illustrated.

shared proton that is stabilized through a N–H–N hydrogen bond. The two planar pyridine rings in the ligand are connected through a carbon–carbon single bond providing a torsional degree of freedom to the system that acts as a gating mode and regulates the donor–acceptor hydrogen-bond distance. The torsional rotation C–C bond, therefore, influences the basicity or proton affinity of protonated 2,2′-bipyridine. Thus, in this study, the CC torsion angle,  $\theta$ , and the associated relative proton position along the donor–

acceptor axis, *x*, are both probed using the formalism presented above, and depicted in Figure 13. Thus,

$$\hat{H} = \frac{-\hbar^2}{2m} \frac{\partial^2}{\partial x^2} + \frac{-\hbar^2}{2m} \frac{\partial^2}{\partial (a\theta)^2} + V(x, \theta)$$
(44)

where we have absorbed  $(a\theta)$  into the derivative operation to emphasize the Cartesian nature of the cylindrical angle  $d(a\theta) = ad\theta$ . Using the TN framework for time-evolution coupled with regularization developed above, in this section, we inspect the quantum dynamics of the shared proton and organize it as follows. Section V A is dedicated to introduce the Hamiltonian operator describing the molecular system, and is complemented by Supporting Information. We first present an abridged discussion on the two-dimensional potential surface driving the interactions, the electronic structure methods used to obtain it, and its corresponding TN decomposition (MPO). The kinetic energy component of the Hamiltonian is then described along with the representation used to write the operator. In Section V B, we present a detailed discussion of the numerical simulations and the benchmarking methods used to compare the numerical results.

**V.A.** The Nuclear Hamiltonian and the Dimensionally Reduced PES. In a cylindrical coordinate system, the 2,2'-bipyridine molecule is described by two relevant nuclear degrees of freedom, which are defined in eq 44. First, the cylindrical angle  $\theta$ , (dihedral angle in the molecular frame as shown in Figure 13) described by the planarity of the two pyridyl rings around the C–C bond, which modulates the donor–acceptor distance, i.e., the internuclear separation between the two nitrogen atoms. Second, the relative position x of the shared hydrogen nucleus along the NN direction.

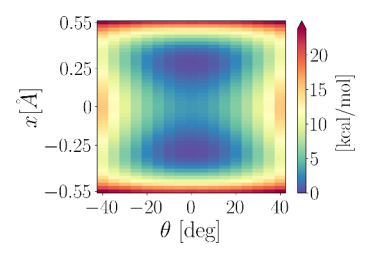
The potential energy surface is hence reduced to a twodimensional scalar function  $V(x, \theta)$ , and computed through electronic structure calculations (see Supporting Information for more details). The details regarding the number of grid points and the level of theory employed are provided in Table 1. The obtained function  $V(x, \theta)$  is a symmetric, double-well

Table 1. Characteristics of the Grid over Which the 2D Potential Surface Is Created

parameter	value		
no. of grid points along the <i>x</i> -dimension	50		
no. of grid points along the $\theta$ -dimension	17		
grid size along the $x$ -dimension $[\mathring{A}]$	1.1		
range of angles along the $\theta$ -dimension	[-40°, 40°]		
level of theory	B3LYP/6-311++G(d,p)//B3LYP/ 6-311++G(d,p)		

anharmonic potential and it is depicted in Figure 14. In a manuscript under preparation, we discuss the tensor network based quantum dynamics of such systems implemented on the IonQ ion-trap quantum computing system.

The kinetic energy is approximated using the distributed approximating functionals (DAF). The result is an efficient banded Toeplitz structure that takes the following analytic closed-form expression



**Figure 14.** Colormap plot of the PES for the protonated 2,2'-bipyridine system. The two dimensions, x and  $\theta$ , correspond to the vibrational degree of freedom of transferring proton along the internuclear axis joining the two nitrogen atoms, and the torsional degree of freedom due to planar rotations of the pyridyl rings about the C–C bond.

$$K(y) = \frac{-\hbar^2 e^{-y^2}}{4m\sigma_0^3 \sqrt{2\pi}} \sum_{k=0}^{M_{\text{DAF}}/2} \frac{1}{k!} \left(-\frac{1}{4}\right)^k H_{2k+2}(y)$$
(45)

where  $y \equiv (x_j - x_j')/\sqrt{2}\,\sigma_0$ , with  $x_j$  and  $x_j'$ , generically representing two grid points along the two dimensions referred to above as x and  $\theta$ . The quantity,  $H_{2k+2}(y)$  are the even-order Hermite polynomials that uniquely depend on the separation between grid points along each dimension. The accuracy of the approximation is tuned via the variational parameters  $M_{\rm DAF}$  and  $\sigma_0$ . The aforementioned banded Toeplitz structure is critical in computing a direct map to quantum simulators as discussed in ref 192.

With the PES and kinetic energies defined, the propagators and hence the Trotterized time-evolution operator of eq 10 are then straightforward to construct for lower dimensional quantum problems; especially considering the PES is diagonal in the position basis.

V.B. Numerical Simulation of Quantum Dynamics. We choose exact diagonalization of the nuclear Hamiltonian (eq 9) as our benchmarking method. Error estimates are based on expressions provided in the Supporting Information, and are based on the Frobenius norm of the difference between the MPS approximations and the exact results. The initial quantum state for the shared proton is chosen in four ways and the respective parameters are shown in Table 2: (a) A two-dimensional Gaussian wavepacket positioned at the grid center with 4 tunable parameters chosen in such a way that the lower eigenenergies of the Hamiltonian have significant contributions. (b) A thermal wavepacket with thermal weight for eigenstates chosen at temperatures T = 300 K and T = 600 K. (c) A product state with ground eigenstate of one-dimensional Hamiltonian along x-direction and a constant function along  $\theta$ -direction.

V.B.1. Error Analysis for Tensor Network Factorization of the Potential Propagator. The first step toward performing quantum nuclear dynamics with tensor networks involves the creation of the various tensor cores in eq 13. However, note that in Eq. 13, as in eqs 4a to 4c, for ease of notation, the tensor cores have been rescaled as

$$V_{\beta_1}^{[1]x_1} \sqrt{\tilde{\lambda}_{\beta_1}^{[1]}} \to V_{\beta_1}^{[1]x_1}$$
 (46a)

$$\sqrt{\tilde{\lambda}_{\beta_{j-1}}^{[j-1]}} \mathcal{V}_{\beta_{j-1}\beta_{j}}^{[j]x_{j}} \sqrt{\tilde{\lambda}_{\beta_{j}}^{[j]}} \to \mathcal{V}_{\beta_{j-1}\beta_{j}}^{[j]x_{j}}$$

$$\tag{46b}$$

$$\sqrt{\tilde{\lambda}_{\beta_{N}}^{[N]}} \mathcal{V}_{\beta_{N-1}}^{[N]x_{N}} \to \mathcal{V}_{\beta_{N-1}}^{[N]x_{N}}$$
 (46c)

Table 2. Initial Wavefunction Characteristics

initial wavepacket $(t=0)$ $\psi(\overline{\mathbf{x}}; 0)$	GS population $ \langle \chi_0   \psi \rangle ^2$	$\begin{array}{c} \text{SVR} \\ \text{threshold} \\ \boldsymbol{\varepsilon}_{\text{SVR}} \end{array}$	truncated bond dimension Γ	parameters	average energy [kcal/mol]
$\psi_{G}(\overline{\mathbf{x}}; 0) = \frac{1}{2\pi\sigma_{x}^{2}\sigma_{\theta}^{2}} \exp\left[-\frac{(x - \mu_{x})^{2}}{2\sigma_{x}^{2}} - \frac{(\theta - \mu_{\theta})^{2}}{2\sigma_{\theta}^{2}}\right]$	91.2%	_	1	$\sigma_x = 0.25 \text{ Å}, \ \mu_x = 0.55 \text{ Å}, \ \sigma_\theta = 16.99^{\circ}, \ \mu_\theta = 0.0^{\circ}$	4.422
$\psi_{T}(\overline{\mathbf{x}}; 0) = \sum_{j} \exp[-E_{j}/kT]\chi_{j}(x, \theta)$	91.6%	10 <sup>-7</sup>	7	T = 300K	3.952
$\psi_{T}(\overline{\mathbf{x}}; 0) = \sum_{j} \exp[-E_{j}/kT]\chi_{j}(x, \theta)$	76.6%	10 <sup>-7</sup>	7	T = 600K	4.067
$\psi_{\mathbb{C}}(\overline{\mathbf{x}}; 0) = \chi_0(x, \theta = 0^\circ) \times \mathbb{C}$	68.2%	_	1	$C = 1/\sqrt{17}$	9.339

In addition, the set of singular values above serve as an indicator of the entanglement between the physical dimensions. As a result,  $\beta_k$  may not encompass the full range of available singular values but rather includes states that are most significant to the creation of the original function,  $\psi(\bar{\mathbf{x}}; t)$ . This sets the limit on the bond dimension,  $\eta_k$  and is determined here using a singular value ratio (SVR) truncation method, <sup>18,220</sup> briefly described in Supporting Information. The error associated with such a truncation is proportional to the sum of the squares of the discarded singular values (See Supporting Information and refs 18, 220. for a detailed discussion). Due to its diagonal form, the error in the MPO approximation to the potential propagator is the  $L_2$ -norm of the difference vector between the MPO version of the potential propagator and the full-grid (exponential scaling) potential energy propagator, and given in Supporting Information.

In Figure 15(a), we show that the bond dimension increases as the SVR cutoff is varied. The associated error with the TN

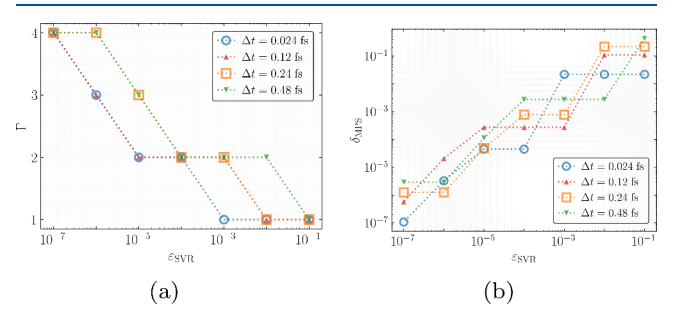


Figure 15. Figure (a): Number of singular values retained for different threshold parameters  $\varepsilon_{\text{SVR}}$  (see Supporting Information) at different time-steps  $\Delta t$ . Figure (b): Error in the TN approximation of the potential propagator  $\exp[-iV(\overline{\mathbf{x}})\Delta t/2\hbar]$ , see Supporting Information, as a function of the threshold parameter  $\varepsilon_{\text{SVR}}$  at different time-steps  $\Delta t$ .

approximation of the potential propagator  $\exp[-iV(\overline{\mathbf{x}})\Delta t/\hbar]$  (see eq 13), is computed according to eq (SI-10) in Supporting Information and illustrated in Figure 15(b) as a function of  $\varepsilon_{\text{SVR}}$ , which as noted above, yields a user defined tolerance parameter that determines the number of singular values retained in the SVD, namely, the bond dimension  $\Gamma$ . (see eq 41 and associated discussion). Additionally, since the timestep  $\Delta t$  is a key parameter in the time-evolution operator, and a source of error due to Trotter, we present all our results at four different time-steps  $\Delta t = 0.024$ , 0.12, 0.24, and 0.48 fs. Since typical hydrogen bond vibrational frequencies have a

time-period in the few femtoseconds range, these time-steps provide an adequate set of benchmarks for our algorithm.

From Figures 15(a) and 15(b), we see that the optimal bond dimension of the potential propagator will depend on the timestep chosen; small  $\Delta t$  will allow a higher compression rate with an acceptable approximation error, that is, the bond dimension  $\Gamma$  is significantly smaller for small time-steps. Moreover, as the error associated with the Trotter approximation is  $O(\Delta t^2)$ , small  $\Delta t$  is also favorable for precision. The downside, however, comes from the multiple intermediate steps needed to propagate the wave function at a finite time  $t = N_t \Delta t$ . Since the bond dimension must be regularized at some frequency for large  $N_t$ , this is computationally challenging, especially for large dimensional systems. Therefore, the choice of  $\Delta t$  must be a suitable compromise between the initial compression, the Trotter error, and the number of time-steps required.

V.B.2. Regularized Tensor Network Propagation. The effectiveness of the tensor-network rank-reduction algorithm presented here is seen from Figure 16. The exponential growth

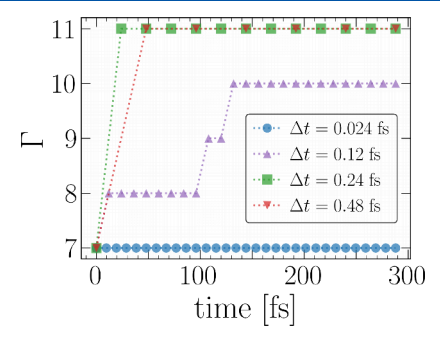


**Figure 16.** Regularized bond dimension  $\Gamma$  as a function of propagation time. Results corresponding to the propagated thermal wavepacket at  $T=300~{\rm K}$  with a threshold parameter of  $\varepsilon_{\rm SVR}=10^{-7}$ .

of the unregularized bond dimension in Figure 8, explicitly illustrates how the naive implementation of the time-evolution of TN states, may quickly render the computation unmanageable. Using a fixed threshold  $\varepsilon_{\rm SVR}$ , our QR-SVD regularization scheme (Figure 16) effectively maintains a consistent bond dimension for the propagated state throughout the entire time evolution.

In Figure 17, we show the population exchange between different eigenstates as a function of time by projecting the time-evolved wavepackets (tensor network and direct diagonalization) onto the eigenstates of the system. The oscillations in Figure 17 is of course an expected result with frequencies that are determined by the respective eigenenergies of the

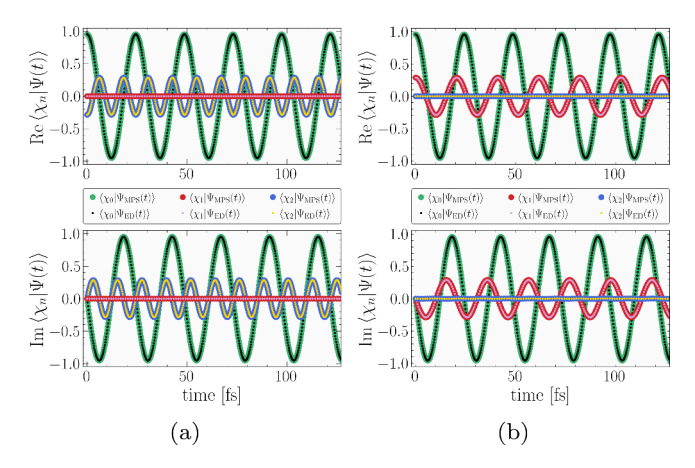


**Figure 17.** Time-evolution of the eigenstate population. Projection of the time-dependent MPS-wavepacket with QR-SVD regularization, onto the first three eigenstates of the nuclear Hamiltonian. Exact diagonalization (ED) results are shown for comparison. The Gaussian wavepacket was used as initial wave function in (a) and the  $T=300~{\rm K}$  thermal wavepacket in (b). The time-step size in both figures is  $\Delta t=0.24~{\rm fs}$ .

states onto which the time-dependent wavepackets are projected; but Figure 17 portrays the agreement with the tensor network and exact diagonalization results.

In Figure 18, we present the wavepacket survival amplitude,  $\langle \Psi(0)|\Psi(t)\rangle$ . Here once more, the QR-SVD regularization

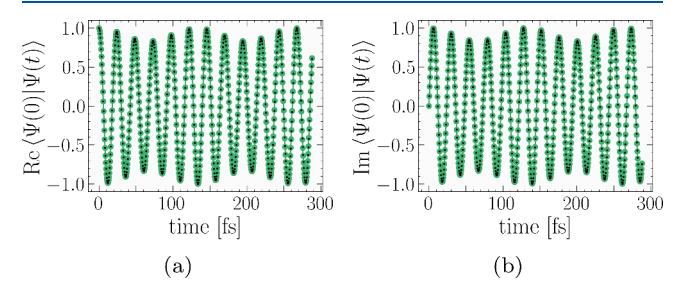


Figure 18. Survival amplitudes of the time-dependent wavepacket evolving on a two-dimensional potential energy surface as obtained from the TN propagation with QR-SVD regularization algorithm (green line) and its comparison with exact diagonalization (ED) of nuclear Hamiltonian (black dots), including the real (a) and imaginary parts (b). The initial wavepacket chosen is  $\psi_T(\overline{\mathbf{x}}; 0)|_{T=300\text{K}}$  and time-step size is  $\Delta t = 0.24$  fs.

algorithm completely captures the wavepacket oscillations with an error, defined as  $\|\langle \Psi(0)|\Psi(t)\rangle_{ED} - \langle \Psi(0)|\Psi(t)\rangle_{MPS}\|_2$ , of the order of  $10^{-3}$ .

The time-averaged error  $\overline{\Delta \Psi}_{MPS}$  in the regularized TN approximation, given by the expression

$$\overline{\Delta \Psi}_{\text{MPS}} = \frac{1}{\tau} \int_0^{\tau} dt \sqrt{\frac{1}{N_{\overline{\mathbf{x}}}} \int d\overline{\mathbf{x}} || \psi(\overline{\mathbf{x}}; t) - \psi_{\text{MPS}}(\overline{\mathbf{x}}; t) ||^2}$$
(47)

where  $\psi$  is the benchmark time-evolved state,  $\psi_{\text{MPS}}$  the propagated MPS wave function, and  $\tau$  is the total time of propagation, is mentioned in Table 3 as a function of time-step  $\Delta t$ . The most important feature of Table 3 is the fact that all differences between  $\psi_{\rm ED}$  and  $\psi_{\rm MPS}$ , are very close to each other at each time-step. This shows that the initial truncation in the TN decomposition of both, the potential propagators and the initial wave functions, are good approximations; and that the regularization has successfully pruned the artificial entanglement introduced by the time-evolution, resulting in numerical precision close to the exact diagonalization results. However, it is crucial to note that each SVD truncation introduces additional errors, and these errors typically accumulate over time. Additionally, mitigating such errors necessitates higher ranks in bond dimensions, which inevitably increase over time. Our goal here is to find a good compromise between accuracy and efficiency to allow stable longer-term dynamics.

In Table 3, we also show the extent to which the total energy is conserved for long time dynamics of the order of several femtoseconds. For different time-step  $\Delta t$ , the energy conservation is probed by computing the absolute difference between the time-averaged energies and the energy at each time-step. The root-mean square error for different propagating time-steps  $\Delta t$  is shown in Table 3. These results reside well within the subkcal/mol range needed for accurate dynamics. It must be noted that for large dimensional systems, dynamics at these time scales, would be impossible to do without the regularization scheme presented here, even though the TN approach reduces the exponential complexity of quantum dynamics.

V.B.3. Vibrational Spectral Behavior from Time-Evolution of Any Initial State. The computation of the shared-proton wavepacket dynamics provides a means to accurately determine its vibrational frequencies and is given by the Fourier transform of the density—density time autocorrelation function,  $\text{Tr}[\rho(0)\rho(t)]$  as

Table 3. Root Mean Square Error in Wavepacket Energy,  $\Delta E$  [kcal/mol], and Time Averaged Error between the TN Propagated Wavefunction with QR-SVD Regularization and with Propagation via Exact Diagonalization of the Nuclear Hamiltonian,  $\overline{\Delta \Psi}_{MPS}$ , for Different Propagating Time-Steps  $\Delta t$  and Different Initial Wavefunction Chosen

		ΔE [kcal/mol]			$\overline{\Delta\Psi}_{ ext{MPS}}$	
$\Delta t$ [fs]	$\psi_G(\overline{\mathbf{x}}; 0)$	$\psi_T(\overline{\mathbf{x}}; 0) _{T=300\mathrm{K}}$	$\psi_T(\overline{\mathbf{x}}; 0) _{T=600\mathrm{K}}$	$\psi_G(\overline{\mathbf{x}}; 0)$	$\psi_T(\overline{\mathbf{x}}; 0) _{T=300\mathrm{K}}$	$\psi_T(\overline{\mathbf{x}}; 0) _{T=600\mathrm{K}}$
0.024	$5.42 \times 10^{-6}$	$4.70 \times 10^{-8}$	$3.20 \times 10^{-7}$	$3.22 \times 10^{-6}$	$2.67 \times 10^{-6}$	$2.83 \times 10^{-6}$
0.12	$1.39 \times 10^{-4}$	$4.51 \times 10^{-7}$	$7.94 \times 10^{-6}$	$8.08 \times 10^{-5}$	$6.72 \times 10^{-5}$	$7.11 \times 10^{-5}$
0.24	$1.53 \times 10^{-3}$	$2.52 \times 10^{-5}$	$4.54 \times 10^{-5}$	$3.27 \times 10^{-4}$	$2.70 \times 10^{-4}$	$2.86 \times 10^{-4}$
0.48	$3.18 \times 10^{-3}$	$7.31 \times 10^{-4}$	$9.18 \times 10^{-4}$	$1.35 \times 10^{-3}$	$1.09 \times 10^{-3}$	$1.15 \times 10^{-3}$

$$\int_{-\infty}^{+\infty} dt e^{i\omega t} \operatorname{Tr}[\rho(0)\rho(t)] = \int_{-\infty}^{+\infty} dt e^{i\omega t} \operatorname{Tr}\left[|\chi(0)\rangle\langle\chi(0)|\sum_{i,j} c_i(0)c_j^*(0)e^{i(E_i - E_j)t/\hbar}|\phi_i\rangle\langle\phi_j|\right]$$

$$= \sum_{i,j} |c_i(0)|^2 |c_j(0)|^2 \delta(\omega - (E_i - E_j)/\hbar)$$
(48)

One may rewrite this using the convolution theorem<sup>221</sup> as

$$\int dx \left\{ \left| \int_{-\infty}^{+\infty} dt e^{i\omega t} \sum_{i,j} c_{i}(0) c_{j}^{*}(0) e^{i(E_{i} - E_{j})t/\hbar} \phi_{i}(x) \phi_{j}(x) \right| \right\}^{2} + \int_{x \neq x'} dx dx' \left| \int_{-\infty}^{+\infty} dt e^{i\omega t} \sum_{i,j} c_{i}(0) c_{j}^{*}(0) e^{i(E_{i} - E_{j})t/\hbar} \phi_{i}(x) \phi_{j}(x') \right|^{2}$$
(49)

While standard approaches may compute the results from eq 49, a quantum computer, such as that utilized in ref 61., has the ability to obtain information at a finer resolution and compute the individual terms inside the integral above as, for example,

$$I(\omega) = \int_{-\infty}^{+\infty} dt e^{i\omega t} \sum_{i,j} c_i(0) c_j^*(0) e^{i(E_i - E_j)t/\hbar} \phi_i(x) \phi_j(x)$$

$$= \sum_{i,j} \delta(\omega - (E_i - E_j)) c_i(0) c_j^*(0) \phi_i(x) \phi_j(x)$$
(50)

separately. By measuring eq 50 on an ion-trap quantum computer in ref 61, we have provided a new approach to determine spectroscopic features in complex systems using quantum computing platforms. Here, we use eq 50 to compute vibrational properties.

In Figure 19, we show the vibrational frequencies obtained from the Fourier transform of the time-evolution of the initial wavepackets as mentioned in Table 2. The vibrational energies

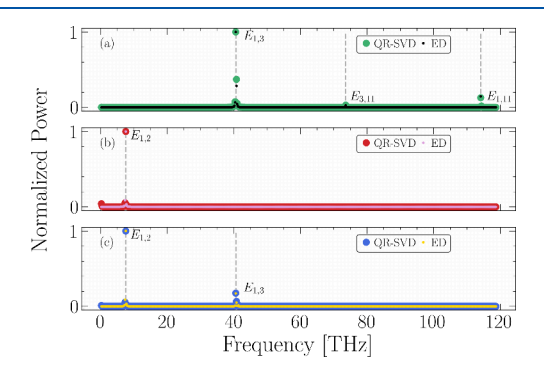


Figure 19. Frequency spectra of a shared-proton in 2,2'-bipyridine. (a)-(c) The time evolution wavepacket obtained from the TN propagation with QR-SVD regularization algorithm (empty circles) and its comparison with exact diagonalization (ED) of nuclear Hamiltonian (filled circles) are Fourier-transformed to reveal frequency spectra of the shared-proton oscillation. Each peak corresponds to a frequency splitting between eigenstates of the discrete nuclear Hamiltonian. Dashed gray lines and labels show predicted frequencies from exact diagonalization of the nuclear Hamiltonian. The initial wavepackets chosen in (a)-(c) are  $\psi_G(\overline{\mathbf{x}}; 0)$ ,  $\psi_T(\overline{\mathbf{x}}; 0)|_{T=300\mathrm{K}}$  and  $\psi_T(\overline{\mathbf{x}}; 0)|_{T=600\mathrm{K}}$  respectively as mentioned in Table 2.

obtained from the time dynamics are compared to the exact diagonalization results (dashed gray lines). The TN propagation with QR-SVD regularization algorithm captures the vibrational spectra of the protonated 2,2'-bipyridine molecule within an uncertainty of 3 cm<sup>-1</sup> wavenumbers which is well within the range of spectroscopic accuracy for such molecular vibration problems.

V.B.4. Numerically Controlling the Entanglement Across Quantum Dimensions through Tensor Network Form of the Potential Propagator. The construction of a tensor network approximation for the potential for systems with arbitrary number of degrees of freedom, such as that discussed above, may, in general, be an exponential scaling task. In this respect, in ref 60., the authors introduce an approach to directly obtain a TN form of the post-Hartree—Fock potential surface and associated potential propagator from a graph-theoretically generated molecular fragmentation and many-body scheme for post-Hartree—Fock electronic structure potential surfaces. Such approaches can be naturally integrated with the approach here to reduce the computational cost arising from the creation of the various tensor cores in eqs 11 and 12.

Correspondingly, the first two surviving singular vectors for the matrix product decomposition of the potential propagator are shown in Figure 20 as a function of its respective physical dimensions x and  $\theta$ . As can be seen from eqs 11 and 12, the probabilistic contribution of each product state within the tensor network,

$$\mathcal{V}_{x\theta}^{x'\theta'} = \sum_{\beta_1} \mathcal{V}_{\beta_1}^{[1]x'x} \mathcal{V}_{\beta_1}^{[2]\theta'\theta} \delta_x^{x'} \delta_{\theta}^{\theta'}$$

$$\tag{51}$$

toward quantum propagation may be seen as arising from the respective norms with respect of x and  $\theta$ ,

$$\|\mathcal{V}_{\beta_{1}}^{[1]x}\|_{2}\|\mathcal{V}_{\beta_{1}}^{[2]\theta}\|_{2} \tag{52}$$

That is, eq 52 depicts the contribution from a specific product state in the tensor network decomposition, eqs 11, 12, and 51, toward quantum propagation, and this modulates the degree of correlation that is present within the quantum system. This is because, the weights afforded to quantum propagation by each product state, as given by eq 52, results in correlations across dimensions. A critical hallmark of the approach here is that such entanglement or correlation is discovered through firstprinciples electronic structure and not predetermined by choice of model potential used. Consequently, it may be noted from Figure 20 that it appears that the contribution toward quantum propagation from the second product state is approximately three-orders of magnitude smaller as compared to the first product state. Thus the degree of entanglement between these dimensions is limited, and in an accompanying set of papers, we describe experimental and theoretical evidence where this system is simulated on an ion-trap quantum computer, and molecular vibrations are captured in an extremely accurate manner by the quantum simulation.

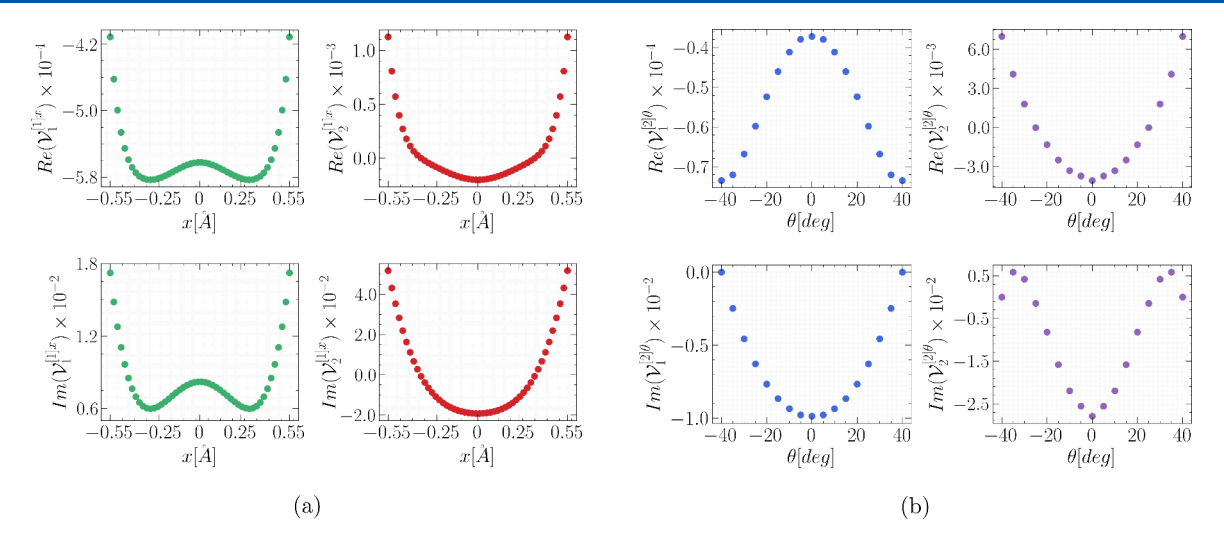


Figure 20. TN decomposition of the potential propagator. Real and imaginary parts of the first two singular vectors  $\mathcal{V}_{\beta_k}^{[k]}$  as a function of the physical dimensions x (represented as superscript in the vertical axes) and  $\theta$  (represented as superscript in the vertical axes). The time-step length is taken as  $\Delta t = 0.024$  fs. (The Re( $\mathcal{V}_1^{[1]x}$ ) values are shifted by 0.763 while Re( $\mathcal{V}_1^{[2]\theta}$ ) values are shifted by 1.3095).

Viewed in this manner, there is an exchange of population between the family of states,

$$\left\{ \int dx \sum_{\alpha_{1}} \mathcal{V}_{\beta_{1}}^{[1]x'x} \phi_{\alpha_{1}}^{[1]x} \right\}_{\beta_{1}}$$
(53)

and

$$\left\{ \int d\theta \sum_{\alpha_1} \mathcal{V}_{\beta_1}^{[2]\theta'\theta} \phi_{\alpha_1}^{[2]\theta} \right\}_{\beta_1} \tag{54}$$

as per eq 37 at every step of quantum propagation, and this exchange of population *entangles* the two dimensions, if this population exchange arises from the multiconfigurational, nonproduct, nature of the potential indicated by eqs 12 and 13. For example, the norms in eq 52 are responsible for reducing or raising the relative probabilities within the states in eqs 53 and 54 thus yielding an exchange in population. In fact, this can be seen in Figure 21, where the initial wave function is

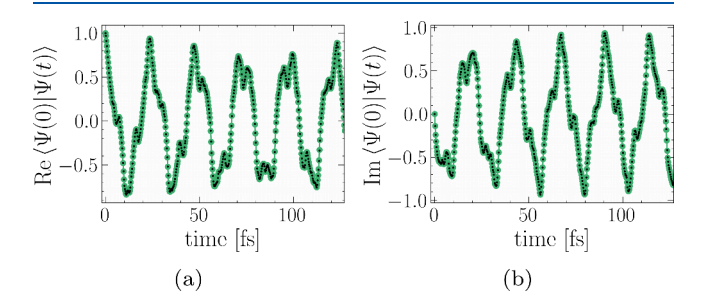


Figure 21. Survival amplitudes of the time-dependent wavepacket evolving on a two-dimensional potential energy surface as obtained from the TN propagation with QR-SVD regularization algorithm (green line) and its comparison with exact diagonalization (ED) of nuclear Hamiltonian (black dots), including the real (a) and imaginary parts (b). As the initial wavepacket chosen is the product state  $\psi_C(\mathbf{x}; 0)$  mentioned in Table 2, the figure depicts the exchange of population between the two-dimensions. The time-step size is  $\Delta t = 0.24$  fs.

a product state  $\psi_{\mathbb{C}}(\overline{\mathbf{x}};0)$  mentioned in Table 2. The wave function along x-direction is a ground state of the one-dimensional Hamiltonian along x-direction at  $\theta=0^\circ$ , while the wave function is chosen to be constant along  $\theta$  direction. Hence its time-evolution with time allows us to gauge the extent to which the potential couples the dimensions which will result in population exchange and entanglement across dimensions, the latter being manifested through the change in  $\Gamma$ . It must be noted that such an exchange in population only arises due to the entanglement as captured within the potential.

## VI. CONCLUSIONS

In this paper, we introduce (a) an efficient method for the simulation of multidimensional quantum nuclear dynamics based on the TN representation of the wave function and the unitary time-evolution operator, and (b) a general quantum circuit approach for tensor network based quantum nuclear dynamics. Using the proposed regularization algorithm of the bond dimension, which is the core of this work, we are able to reconstruct an efficient MPS representation of the propagated wave function, by removing numerical redundancies that otherwise will grow exponentially with time, therefore gauging the true entanglement dimension on the fly. One advantage of our approach is that all matrix operations can be executed in parallel, reducing significantly the computational time and making the algorithm amenable to quantum-classical implementations. Additionally, the quantum circuit version also allows the algorithm to be implemented on quantum hardware systems. The accuracy of our approach is probed using a protonated 2,2'-bipyridine molecule with two physical degrees of freedom. This low-dimensional system, allows to use time propagation via exact diagonalization of the Hamiltonian as benchmark tool. By computing different quantities such as eigenstate populations, survival amplitudes, energy conservation, and error measures, we show that our TN method of propagation is a powerful and accurate approach.

As TN methods become more useful to simulate quantum circuits and as key components of hybrid algorithms suitable for NISQ hardware, in future publications, we will incorporate

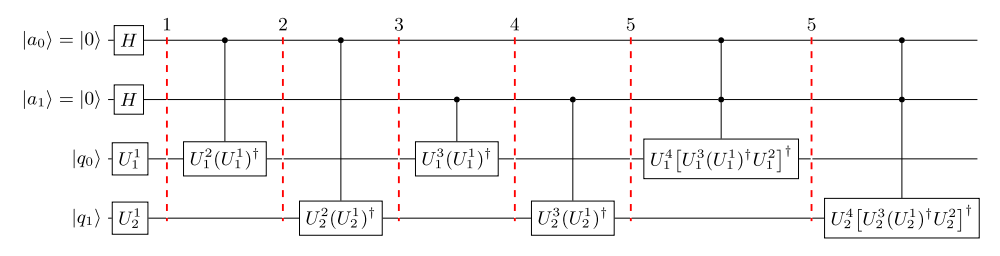


Figure 22. Same as Figure 7 but with individual steps emphasized and complemented by eqs 27 to 29.

a quantum simulation technique in order to build a hybrid approach to quantum simulation that could combine the dimensional reduction of TN with the computational advantages of quantum algorithms.

# ■ APPENDIX A: ELABORATING THE VARIOUS STAGES INVOLVED IN FIGURE 7

As noted in Figure 7, as the entanglement dimensions grow, the circuit gets more complicated. While the number of ancilla needed grow, the complexity of the circuit, in terms of conditionality, also grows resulting in the final state at the end of the circuit in Figure 7. The detailed development of eq 32 and Figure 7 are given below as per Figure 22:

#### Stage 1:

$$\begin{split} &\frac{1}{\sqrt{2}}(|0\rangle+|1\rangle)\otimes\frac{1}{\sqrt{2}}(|0\rangle+|1\rangle)\otimes U_1^{1}|q_0\rangle\otimes U_2^{1}|q_1\rangle\\ &=\frac{1}{2}(|00\rangle+|01\rangle+|10\rangle+|11\rangle)\otimes U_1^{1}|q_0\rangle\otimes U_2^{1}|q_1\rangle \end{split} \tag{A1}$$

#### Stage 2:

$$\begin{split} &\frac{1}{2}(|00\rangle \otimes U_1^1|q_0\rangle \otimes U_2^1|q_1\rangle + |01\rangle \otimes U_1^1|q_0\rangle \otimes U_2^1|q_1\rangle + \\ &|10\rangle \otimes U_1^2|q_0\rangle \otimes U_2^1|q_1\rangle + |11\rangle \otimes U_1^2|q_0\rangle \otimes U_2^1|q_1\rangle) \end{split} \tag{A2}$$

#### Stage 3:

$$\begin{split} &\frac{1}{2}(|00\rangle \otimes U_1^1|q_0\rangle \otimes U_2^1|q_1\rangle + |01\rangle \otimes U_1^1|q_0\rangle \otimes U_2^1|q_1\rangle + \\ &|10\rangle \otimes U_1^2|q_0\rangle \otimes U_2^2|q_1\rangle + |11\rangle \otimes U_1^2|q_0\rangle \otimes U_2^2|q_1\rangle) \end{split} \tag{A3}$$

#### Stage 4:

$$\begin{split} &\frac{1}{2}\langle |00\rangle \otimes U_1^1|q_0\rangle \otimes U_2^1|q_1\rangle + |01\rangle \otimes U_1^3|q_0\rangle \otimes U_2^1|q_1\rangle + \\ &|10\rangle \otimes U_1^2|q_0\rangle \otimes U_2^2|q_1\rangle + \\ &|11\rangle \otimes U_1^3U_1^{\dagger\dagger}U_1^2|q_0\rangle \otimes U_2^2|q_1\rangle ) \end{split} \tag{A4}$$

#### Stage 5:

$$\begin{split} &\frac{1}{2}(|00\rangle \,\otimes\, U_1^1|q_0\rangle \,\otimes\, U_2^1|q_1\rangle \,+\, |01\rangle \,\otimes\, U_1^3|q_0\rangle \,\otimes\, U_2^3|q_1\rangle \,+\\ &|10\rangle \,\otimes\, U_1^2|q_0\rangle \,\otimes\, U_2^2|q_1\rangle \,+\\ &|11\rangle \,\otimes\, U_1^3{U_1^1}^\dagger U_1^2|q_0\rangle \,\otimes\, U_2^3{U_2^1}^\dagger U_2^2|q_1\rangle) \end{split} \tag{A5}$$

#### Stage 6:

$$\begin{split} &\frac{1}{2}(|00\rangle\otimes U_1^1|q_0\rangle\otimes U_2^1|q_1\rangle + |01\rangle\otimes U_1^3|q_0\rangle\otimes U_2^3|q_1\rangle + \\ &|10\rangle\otimes U_1^2|q_0\rangle\otimes U_2^2|q_1\rangle + \\ &|11\rangle\otimes U_1^4|q_0\rangle\otimes U_2^3U_2^{\dagger\dagger}U_2^2|q_1\rangle) \end{split} \tag{A6}$$

and finally

$$\begin{split} &\frac{1}{2}(|00\rangle \otimes U_1^1|q_0\rangle \otimes U_2^1|q_1\rangle + |01\rangle \otimes U_1^3|q_0\rangle \otimes U_2^3|q_1\rangle + \\ &|10\rangle \otimes U_1^2|q_0\rangle \otimes U_2^2|q_1\rangle + |11\rangle \otimes U_1^4|q_0\rangle \otimes U_2^4|q_1\rangle) \end{aligned} \tag{A7}$$

which is the result in eq 32. As in eqs 30 and 31, the respective components of the tensor network as measured outcomes from the ancilla.

## ASSOCIATED CONTENT

# Supporting Information

The Supporting Information is available free of charge at https://pubs.acs.org/doi/10.1021/acs.jpca.4c03407.

We analytically compare our regularization method with that described in ref 199, we discuss the potential energy surface obtained for protonated 2,2'-bipyridine which was studied using the tensor network algorithm described here, and we provide expressions for error estimates for the tensor network form of the potential propagator and the wavepacket that are used in the paper (PDF)

# AUTHOR INFORMATION

## **Corresponding Author**

Srinivasan S. Iyengar — Department of Chemistry, Indiana University, Bloomington, Indiana 47405, United States; Indiana University Quantum Science and Engineering Center (IU-QSEC), Indiana University, Bloomington, Indiana 47405, United States; orcid.org/0000-0001-6526-2907; Email: iyengar@indiana.edu

#### **Authors**

Anurag Dwivedi — Department of Chemistry, Indiana University, Bloomington, Indiana 47405, United States; Indiana University Quantum Science and Engineering Center (IU-QSEC), Indiana University, Bloomington, Indiana 47405, United States

Miguel Angel Lopez-Ruiz — Department of Chemistry, Indiana University, Bloomington, Indiana 47405, United States; Indiana University Quantum Science and Engineering Center (IU-QSEC), Indiana University, Bloomington, Indiana 47405, United States

Complete contact information is available at:

https://pubs.acs.org/10.1021/acs.jpca.4c03407

#### Notes

The authors declare no competing financial interest.

### ACKNOWLEDGMENTS

This study was supported by the National Science Foundation grant Nos. OMA-1936353 and CHE-2102610 to SSI. The authors are grateful to Debadrita Saha, Dr. Anup Kumar, and Dr. Nicole DeGregorio for useful discussions. AD acknowledges support from the John R. and Wendy L. Kindig Foundation.

#### REFERENCES

- (1) Feynman, R. P. Simulating physics with computers. *International Journal of Theoretical Physics* **1982**, 21, 467–488.
- (2) Feynman, R. P.; Hey, J.; Allen, R. W. Feynman Lectures on Computation; Addison-Wesley Longman Publishing Co., Inc., 1998.
- (3) Bowman, J. M. The Self-Consistent-Field Approach to Polyatomic Vibrations. Acc. Chem. Res. 1986, 19, 202.
- (4) Braams, B. J.; Bowman, J. M. Permutationally invariant potential energy surfaces in high dimensionality. *Int. Rev. Phys. Chem.* **2009**, 28, 577.
- (5) Meyer, H.-D.; Manthe, U.; Cederbaum, L. S. The multiconfigurational time-dependent Hartree approach. *Chem. Phys. Lett.* **1990**, *165*, 73–78.
- (6) Wang, X.; Carter, S.; Bowman, J. M. Pruning the Hamiltonian Matrix in MULTIMODE: Test for  $C_2H_4$  and Application to  $CH_3NO_2$  Using a New Ab Initio Potential Energy Surface. *J. Phys. Chem. A* **2015**, *119*, 11632–11640.
- (7) Vendrell, O.; Meyer, H. D. Proton Conduction Along a Chain of Water Molecules. Development of a Linear Model and Quantum Dynamical Investigations Using the Multiconfiguration Time-Dependent Hartree Method. *J. Chem. Phys.* **2005**, *122*, 104505.
- (8) Iyengar, S. S.; Kouri, D. J.; Hoffman, D. K. Particular and Homogeneous Solutions of Time-Independent Wavepacket Schrodinger Equations: Calculations Using a Subset of Eigenstates of Undamped or Damped Hamiltonians. *Theor. Chem. Acc.* 2000, 104, 471
- (9) Tal-Ezer, H.; Kosloff, R. An accurate and efficient scheme for propagating the time dependent Schrödinger equation. *J. Chem. Phys.* **1984**, *81*, 3967.
- (10) Leforestier, C.; Bisseling, R. H.; Cerjan, C.; Feit, M. D.; Freisner, R.; Guldberg, A.; Hammerich, A.; Jolicard, D.; Karrlein, W.; Meyer, H. D.; et al. A Comparison of Different Propagation Schemes for the Time-Dependent Schrödinger Equation. *J. Comput. Phys.* **1991**, *94*, 59.
- (11) Deumens, E.; Diz, A.; Longo, R.; Öhrn, Y. Time-Dependent Theoretical Treatments of the Dynamics of Electrons and Nuclei in Molecular-Systems. *Rev. Mod. Phys.* **1994**, *66*, 917.
- (12) Neuhauser, D.; Baer, M.; Judson, R. S.; Kouri, D. J. The Application of Time-Dependent Wavepacket Methods to Reactive Scattering. *Comput. Phys. Commun.* **1991**, *63*, 460.
- (13) Kouri, D. J.; Huang, Y.; Hoffman, D. K. Iterated Real-Time Path Integral Evaluation Using a Distributed Approximating Functional Propagator and Average-Case Complexity Integration. *Phys. Rev. Lett.* **1995**, *75*, 49.
- (14) Manthe, U.; Meyer, H. D.; Cederbaum, L. S. Wave-packet dynamics within the multiconfiguration Hartree framework: General aspects and application to NOCl. *J. Chem. Phys.* **1992**, *97*, 3199–3213.
- (15) Beck, M. H.; Jäckle, A.; Worth, G. A.; Meyer, H.-D. The multiconfiguration time-dependent Hartree (MCTDH) method: a highly efficient algorithm for propagating wavepackets. *Phys. Rep.* **2000**, *324*, 1–105.

- (16) Meyer, H.-D.; Gatti, F.; Worth, G. A. Multidimensional Quantum Dynamics: MCTDH Theory and Applications; John Wiley & Sons, 2009.
- (17) Otto, F. Multi-layer Potfit: An accurate potential representation for efficient high-dimensional quantum dynamics. *J. Chem. Phys.* **2014**, 140, 014106.
- (18) DeGregorio, N.; Iyengar, S. S. Adaptive Dimensional Decoupling for Compression of Quantum Nuclear Wave Functions and Efficient Potential Energy Surface Representations through Tensor Network Decomposition. *J. Chem. Theory Comput.* **2019**, 15, 2780–2796.
- (19) Wang, H.; Thoss, M. Multilayer formulation of the multiconfiguration time-dependent Hartree theory. *J. Chem. Phys.* **2003**, *119*, 1289–1299.
- (20) Binder, R.; Burghardt, I. First-principles quantum simulations of exciton diffusion on a minimal oligothiophene chain at finite temperature. *Faraday Discuss.* **2020**, 221, 406–427.
- (21) Tucker, L. R. In *Contributions to Mathematical Psychology*; Gulliksen, H., Frederiksen, N., Eds.; Rinehart & Winston, New York, 1964; Chapter The extension of factor analysis to three-dimensional matrices, pp 109–127.
- (22) De Lathauwer, L.; De Moor, B.; Vandewalle, J. A Multilinear Singular Value Decomposition. SIAM Journal on Matrix Analysis and Applications 2000, 21, 1253–1278.
- (23) Orús, R. A practical introduction to tensor networks: Matrix product states and projected entangled pair states. *Ann. Phys.* **2014**, 349, 117–158.
- (24) Chan, G. K.-L.; Keselman, A.; Nakatani, N.; Li, Z.; White, S. R. Matrix product operators, matrix product states, and ab initio density matrix renormalization group algorithms. *J. Chem. Phys.* **2016**, *145*, 014102.
- (25) Orús, R. Tensor networks for complex quantum systems. *Nature Reviews Physics* **2019**, *1*, 538–550.
- (26) Cirac, J. I.; Pérez-García, D.; Schuch, N.; Verstraete, F. Matrix product states and projected entangled pair states: Concepts, symmetries, theorems. *Rev. Mod. Phys.* **2021**, 93, 045003.
- (27) Verstraete, F.; Murg, V.; Cirac, J. Matrix product states, projected entangled pair states, and variational renormalization group methods for quantum spin systems. *Adv. Phys.* **2008**, *57*, 143–224.
- (28) Bridgeman, J. C.; Chubb, C. T. Hand-waving and interpretive dance: an introductory course on tensor networks. *J. Phys. A: Math. Theor.* **2017**, *50*, 223001.
- (29) Montangero, S. Introduction to Tensor Network Methods: Numerical simulations of low-dimensional many-body quantum systems; Springer, Cham, 2018.
- (30) Ran, S.-J.; Tirrito, E.; Peng, C.; Chen, X.; Tagliacozzo, L.; Su, G.; Lewenstein, M. Tensor Network Contractions: Methods and Applications to Quantum Many-Body Systems; Springer, Cham, 2020.
- (31) Silvi, P.; Tschirsich, F.; Gerster, M.; Jünemann, J.; Jaschke, D.; Rizzi, M.; Montangero, S. The Tensor Networks Anthology: Simulation techniques for many-body quantum lattice systems. *SciPost Phys. Lect. Notes* **2019**, DOI: 10.21468/SciPostPhysLectNotes.8.
- (32) Biamonte, J.; Bergholm, V. Tensor Networks in a Nutshell. 2017; DOI: 10.48550/arXiv.1708.00006.
- (33) Biamonte, J. Lectures on quantum tensor networks. 2019; DOI: 10.48550/arXiv.1912.10049.
- (34) Eisert, J. Entanglement and tensor network states. 2013; DOI: 10.48550/arXiv.1308.3318.
- (35) Evenbly, G. A practical guide to the numerical implementation of tensor networks i: Contractions, decompositions, and gauge freedom. *Frontiers in Applied Mathematics and Statistics* **2022**, 8, 806549
- (36) Bañuls, M. C. Tensor network algorithms: A route map. Annual Review of Condensed Matter Physics 2023, 14, 173–191.
- (37) Baiardi, A.; Reiher, M. The density matrix renormalization group in chemistry and molecular physics: Recent developments and new challenges. *J. Chem. Phys.* **2020**, *152*, 040903.

- (38) Buser, M.; Cerrillo, J.; Schaller, G.; Cao, J. Initial system-environment correlations via the transfer-tensor method. *Phys. Rev. A* **2017**, *96*, 062122.
- (39) Kananenka, A. A.; Hsieh, C.-Y.; Cao, J.; Geva, E. Accurate long-time mixed quantum-classical Liouville dynamics via the transfer tensor method. *journal of physical chemistry letters* **2016**, 7, 4809–4814.
- (40) Chenu, A.; Cao, J. Construction of multichromophoric spectra from monomer data: applications to resonant energy transfer. *Physical review letters* **2017**, *118*, 013001.
- (41) Binder, R.; Wahl, J.; Römer, S.; Burghardt, I. Coherent exciton transport driven by torsional dynamics: a quantum dynamical study of phenylene-vinylene type conjugated systems. *Faraday Discuss.* **2013**, 163, 205–222.
- (42) Lubich, C.; Rohwedder, T.; Schneider, R.; Vandereycken, B. Dynamical approximation by hierarchical Tucker and tensor-train tensors. SIAM Journal on Matrix Analysis and Applications 2013, 34, 470–494.
- (43) Frahm, L.-H.; Pfannkuche, D. Ultrafast ab initio quantum chemistry using matrix product states. *J. Chem. Theory Comput.* **2019**, 15, 2154–2165.
- (44) Cazalilla, M.; Marston, J. Time-dependent density-matrix renormalization group: A systematic method for the study of quantum many-body out-of-equilibrium systems. *Physical review letters* **2002**, *88*, 256403.
- (45) Greene, S. M.; Batista, V. S. Tensor-Train Split-Operator Fourier Transform (TT-SOFT) Method: Multidimensional Nonadiabatic Quantum Dynamics. *J. Chem. Theory Comput.* **2017**, *13*, 4034–4042.
- (46) Haegeman, J.; Cirac, J. I.; Osborne, T. J.; Pižorn, I.; Verschelde, H.; Verstraete, F. Time-dependent variational principle for quantum lattices. *Phys. Rev. Lett.* **2011**, *107*, 070601.
- (47) Haegeman, J.; Lubich, C.; Oseledets, I.; Vandereycken, B.; Verstraete, F. Unifying time evolution and optimization with matrix product states. *Phys. Rev. B Condens. Matter* **2016**, *94*, 165116.
- (48) Vidal, G. Efficient classical simulation of slightly entangled quantum computations. *Phys. Rev. Lett.* **2003**, *91*, 147902.
- (49) Verstraete, F.; García-Ripoll, J. J.; Cirac, J. I. Matrix product density operators: simulation of finite-temperature and dissipative systems. *Phys. Rev. Lett.* **2004**, 93, 207204.
- (50) Baiardi, A.; Reiher, M. Large-scale quantum dynamics with matrix product states. *J. Chem. Theory Comput.* **2019**, *15*, 3481–3498.
- (51) DeGregorio, N.; Iyengar, S. S. Challenges in constructing accurate methods for hydrogen transfer reactions in large biological assemblies. *Faraday Discuss.* **2020**, *221*, 379–405.
- (52) Schröder, F. A.; Turban, D. H.; Musser, A. J.; Hine, N. D.; Chin, A. W. Tensor network simulation of multi-environmental open quantum dynamics via machine learning and entanglement renormalisation. *Nat. Commun.* **2019**, *10*, 1062.
- (53) Wang, X.-G.; Carrington, T., Jr A contracted basis-Lanczos calculation of vibrational levels of methane: Solving the Schrödinger equation in nine dimensions. *J. Chem. Phys.* **2003**, *119*, 101–117.
- (54) Bramley, M. J.; Carrington, T., Jr Calculation of triatomic vibrational eigenstates: Product or contracted basis sets, Lanczos or conventional eigensolvers? What is the most efficient combination? *J. Chem. Phys.* **1994**, *101*, 8494–8507.
- (55) Bramley, M. J.; Tromp, J. W.; Carrington Jr, T.; Corey, G. C. Efficient calculation of highly excited vibrational energy levels of floppy molecules: The band origins of H+ 3 up to 35 000 cm-1. *J. Chem. Phys.* **1994**, *100*, 6175–6194.
- (56) Kolda, T. G.; Bader, B. W. Tensor Decompositions and Applications. SIAM Rev. 2009, 51, 455-500.
- (57) Fried, E. S.; Sawaya, N. P. D.; Cao, Y.; Kivlichan, I. D.; Romero, J.; Aspuru-Guzik, A. qTorch: The quantum tensor contraction handler. *PLoS One* **2018**, *13*, No. e0208510.
- (58) Schutski, R.; Lykov, D.; Oseledets, I. Adaptive algorithm for quantum circuit simulation. *Phys. Rev. A* **2020**, *101*, 042335.

- (59) Bauer, B.; Bravyi, S.; Motta, M.; Kin-Lic Chan, G. Quantum Algorithms for Quantum Chemistry and Quantum Materials Science. *Chem. Rev.* **2020**, *120*, 12685–12717.
- (60) Kumar, A.; DeGregorio, N.; Ricard, T.; Iyengar, S. S. Graph-Theoretic Molecular Fragmentation for Potential Surfaces Leads Naturally to a Tensor Network Form and Allows Accurate and Efficient Quantum Nuclear Dynamics. *J. Chem. Theory Comput.* **2022**, 18, 7243.
- (61) Richerme, P.; Revelle, M. C.; Yale, C. G.; Lobser, D.; Burch, A. D.; Clark, S. M.; Saha, D.; Lopez-Ruiz, M. A.; Dwivedi, A.; Smith, J. M.; et al. Quantum computation of hydrogen bond dynamics and vibrational spectra. *J. Phys. Chem. Lett.* **2023**, *14*, 7256–7263.
- (62) Tomesh, T.; Saleem, Z. H.; Perlin, M. A.; Gokhale, P.; Suchara, M. Quantum divide and conquer for combinatorial optimization and distributed computing. *arXiv preprint*. arXiv:2107.07532. 2021.
- (63) Peng, T.; Harrow, A. W.; Ozols, M.; Wu, X. Simulating Large Quantum Circuits on a Small Quantum Computer. *Phys. Rev. Lett.* **2020**, 125, 150504.
- (64) Perlin, M. A.; Saleem, Z. H.; Suchara, M.; Osborn, J. C. Quantum circuit cutting with maximum-likelihood tomography. *npj Quantum Information* **2021**, *7*, 64.
- (65) Tang, W.; Tomesh, T.; Suchara, M.; Larson, J.; Martonosi, M. CutQC: using small Quantum computers for large Quantum circuit evaluations. Proceedings of the 26th ACM International Conference on Architectural Support for Programming Languages and Operating Systems. ASPLOS '21; ACM, 2021.
- (66) Hastings, M. B. An area law for one-dimensional quantum systems. *Journal of Statistical Mechanics: Theory and Experiment* **2007**, 2007, P08024.
- (67) Eisert, J.; Cramer, M.; Plenio, M. B. Colloquium: Area laws for the entanglement entropy. *Rev. Mod. Phys.* **2010**, 82, 277–306.
- (68) Anshu, A.; Harrow, A. W.; Soleimanifar, M. Entanglement spread area law in gapped ground states. *Nat. Phys.* **2022**, *18*, 1362.
- (69) White, S. R. Density matrix formulation for quantum renormalization groups. *Phys. Rev. Lett.* **1992**, *69*, 2863–2866.
- (70) White, S. R. Density-matrix algorithms for quantum renormalization groups. *Phys. Rev. B Condens. Matter* **1993**, 48, 10345–10356.
- (71) Verstraete, F.; Porras, D.; Cirac, J. I. Density matrix renormalization group and periodic boundary conditions: a quantum information perspective. *Phys. Rev. Lett.* **2004**, 93, 227205.
- (72) Schollwöck, U. The density-matrix renormalization group in the age of matrix product states. *Ann. Phys.* **2011**, 326, 96–192.
- (73) Hastings, M. B. Solving gapped Hamiltonians locally. *Phys. Rev. B Condens. Matter* **2006**, 73, 085115.
- (74) Vidal, G. Classical simulation of infinite-size quantum lattice systems in one spatial dimension. *Phys. Rev. Lett.* **2007**, *98*, 070201.
- (75) Daul, S.; Ciofini, I.; Daul, C.; White, S. R. Full-CI quantum chemistry using the density matrix renormalization group. *Int. J. Quantum Chem.* **2000**, *79*, 331–342.
- (76) Mitrushenkov, A. O.; Fano, G.; Ortolani, F.; Linguerri, R.; Palmieri, P. Quantum chemistry using the density matrix renormalization group. *J. Chem. Phys.* **2001**, *115*, 6815–6821.
- (77) Mitrushenkov, A. O.; Linguerri, R.; Palmieri, P.; Fano, G. Quantum chemistry using the density matrix renormalization group II. *J. Chem. Phys.* **2003**, *119*, 4148–4158.
- (78) Chan, G. K.-L. An algorithm for large scale density matrix renormalization group calculations. *J. Chem. Phys.* **2004**, *120*, 3172–3178.
- (79) Chan, G. K.-L.; Kállay, M.; Gauss, J. State-of-the-art density matrix renormalization group and coupled cluster theory studies of the nitrogen binding curve. *J. Chem. Phys.* **2004**, *121*, 6110–6116.
- (80) Szalay, S.; Pfeffer, M.; Murg, V.; Barcza, G.; Verstraete, F.; Schneider, R.; Legeza, O. Tensor product methods and entanglement optimization for ab initio quantum chemistry. *Int. J. Quantum Chem.* **2015**, *115*, 1342–1391.
- (81) Baiardi, A.; Stein, C. J.; Barone, V.; Reiher, M. Optimization of highly excited matrix product states with an application to vibrational spectroscopy. *J. Chem. Phys.* **2019**, *150*, 094113.

- (82) Rakhuba, M.; Oseledets, I. Calculating vibrational spectra of molecules using tensor train decomposition. *J. Chem. Phys.* **2016**, *145*, 124101
- (83) Baiardi, A.; Stein, C. J.; Barone, V.; Reiher, M. Vibrational Density Matrix Renormalization Group. *J. Chem. Theory Comput.* **2017**, *13*, 3764–3777.
- (84) Glaser, N.; Baiardi, A.; Reiher, M. Tensor Network States for Vibrational Spectroscopy. In *Vibrational Dynamics of Molecules*; WORLD SCIENTIFIC, 2021; pp 80–144.
- (85) Liu, Y.; Li, W.-J.; Zhang, X.; Lewenstein, M.; Su, G.; Ran, S.-J. Entanglement-based feature extraction by tensor network machine learning. Frontiers in Applied Mathematics and Statistics 2021, 7, 716044.
- (86) Liu, J.; Li, S.; Zhang, J.; Zhang, P. Tensor networks for unsupervised machine learning. *Phys. Rev. E* **2023**, *107*, L012103.
- (87) Stoudenmire, E.; Schwab, D. J. Supervised learning with tensor networks. Adv. Neural Inf. Process. Syst. 2016, 29.
- (88) Preskill, J. Quantum Computing in the NISQ era and beyond. *Quantum* **2018**, 2, 79.
- (89) Chia, N.-H.; Chung, K.-M.; Lai, C.-Y. On the Need for Large Quantum Depth. *Proceedings of the 52nd Annual ACM SIGACT Symposium on Theory of Computing. STOC 2020*; Association for Computing Machinery, New York, NY, USA: New York, NY, USA, 2020; p 902–915.
- (90) Zhang, J. H.; Iyengar, S. S. Graph-\$\ket{Q}\splangle{C}\vert \$: A Graph-based Quantum-classical algorithm for efficient electronic structure on hybrid quantum/classical hardware systems: Improved quantum circuit depth performance. J. Chem. Theory Comput. 2022, 18, 2885.
- (91) Iyengar, S. S.; Zhang, J. H.; Saha, D.; Ricard, T. C. Graph-\$\\ket{Q}\splangle{C}\vert\$: A Quantum Algorithm with Reduced Quantum Circuit Depth for Electronic Structure. *J. Phys. Chem. A* **2023**, *127*, 9334.
- (92) Preskill, J. Quantum computing 40 years later. arXiv. arXiv:2106.10522. 2021.
- (93) Preskill, J. Quantum computing and the entanglement frontier *arXiv*. arXiv:1203.5813. 2012.
- (94) Campbell, E. T.; Terhal, B. M.; Vuillot, C. Roads towards fault-tolerant universal quantum computation. *Nature* **2017**, *549*, 172–179.
- (95) Harrow, A. W.; Montanaro, A. Quantum computational supremacy. *Nature* **2017**, *549*, 203–209.
- (96) Haghshenas, R.; Gray, J.; Potter, A. C.; Chan, G. K.-L. Variational Power of Quantum Circuit Tensor Networks. *Phys. Rev. X* **2022**, *12*, 011047.
- (97) Di Paolo, A.; Baker, T. E.; Foley, A.; Sénéchal, D.; Blais, A. Efficient modeling of superconducting quantum circuits with tensor networks. *npj Quantum Information* **2021**, *7*, 11.
- (98) Pan, F.; Zhou, P.; Li, S.; Zhang, P. Contracting Arbitrary Tensor Networks: General Approximate Algorithm and Applications in Graphical Models and Quantum Circuit Simulations. *Phys. Rev. Lett.* **2020**, *125*, 060503.
- (99) Foss-Feig, M.; Ragole, S.; Potter, A.; Dreiling, J.; Figgatt, C.; Gaebler, J.; Hall, A.; Moses, S.; Pino, J.; Spaun, B.; et al., Entanglement from tensor networks on a trapped-ion QCCD quantum computer. *arXiv e-prints. arXiv preprint.* arXiv:2104.11235. 2021.
- (100) Nguyen, T.; Lyakh, D.; Dumitrescu, E.; Clark, D.; Larkin, J.; McCaskey, A. Tensor Network Quantum Virtual Machine for Simulating Quantum Circuits at Exascale. *arXiv* preprint. arXiv:2104.10523. 2021.
- (101) Markov, I. L.; Shi, Y. Simulating Quantum Computation by Contracting Tensor Networks. SIAM J. Comput. 2008, 38, 963–981.
- (102) Vincent, T.; O'Riordan, L. J.; Andrenkov, M.; Brown, J.; Killoran, N.; Qi, H.; Dhand, I. Jet: Fast quantum circuit simulations with parallel task-based tensor-network contraction. *arXiv* preprint. arXiv:2107.09793. 2021.
- (103) Levental, M. Tensor networks for simulating quantum circuits on FPGAs. *arXiv preprint*. arXiv:2108.06831. 2021.

- (104) Barratt, F.; Dborin, J.; Bal, M.; Stojevic, V.; Pollmann, F.; Green, A. G. Parallel quantum simulation of large systems on small NISQ computers. *npj Quantum Information* **2021**, *7*, 79.
- (105) Cao, C.; Lackey, B. Quantum Lego: Building Quantum Error Correction Codes from Tensor Networks. *arXiv preprint*. arXiv:2109.08158. 2021.
- (106) Jozsa, R. On the simulation of quantum circuits. *arXiv preprint*. arXiv:quant-ph/0603163. 2006.
- (107) Gelß, P.; Klus, S.; Shakibaei, Z.; Pokutta, S. Low-rank tensor decompositions of quantum circuits. *arXiv preprint*. arXiv:2205.09882.
- (108) Arad, I.; Landau, Z. Quantum Computation and the Evaluation of Tensor Networks. SIAM J. Comput. 2010, 39, 3089—3121
- (109) Ferris, A. J.; Poulin, D. Tensor networks and quantum error correction. *Phys. Rev. Lett.* **2014**, *113*, 030501.
- (110) Wyatt, R. E., Zhang, J. Z. H., Eds. Dynamics of Molecules and Chemical Reactions; Marcel Dekker Inc., New York, NY, 1996.
- (111) Leforestier, C.; Wyatt, R. E. Optical Potential for Laser Induced Dissociation. J. Chem. Phys. 1983, 78, 2334.
- (112) Lill, J. V.; Parker, G. Á.; Light, J. C. Discrete Variable Representations and Sudden Models in Quantum Scattering-Theory. *Chem. Phys. Lett.* **1982**, *89*, 483.
- (113) Light, J. C.; Hamilton, I. P.; Lill, J. V. J. Chem. Phys. 1985, 82, 1400.
- (114) Colbert, D. T.; Miller, W. H. A Novel Discrete Variable Representation for Quantum-Mechanical Reactive Scattering Via the S-Matrix Kohn Method. *J. Chem. Phys.* **1992**, *96*, 1982.
- (115) Huang, Y.; Kouri, D. J.; Arnold, M.; Thomas, L.; Marchioro, I.; Hoffman, D. K. Distributed Approximating Function Approach to Time-Dependent Wavepacket Propagation in 3-Dimensions: Atom-Surface Scattering. *Comput. Phys. Commun.* **1994**, *80*, 1.
- (116) Iyengar, S. S.; Parker, G. A.; Kouri, D. J.; Hoffman, D. K. Symmetry-Adapted Distributed Approximating Functionals: Theory and Application to the Ro-Vibrational States of H<sub>3</sub><sup>+</sup>. *J. Chem. Phys.* **1999**, *110*, 10283.
- (117) Roy, P.-N.; Light, J. C. Time-Dependent Hartree Approaches for the Study of Intramolecular Dynamics in Dimer Systems. *J. Chem. Phys.* **2000**, *112*, 10778.
- (118) Östlund, S.; Rommer, S. Thermodynamic limit of density matrix renormalization. *Phys. Rev. Lett.* **1995**, *75*, 3537–3540.
- (119) Fannes, M.; Nachtergaele, B.; Werner, R. F. Finitely correlated states on quantum spin chains. *Commun. Math. Phys.* **1992**, *144*, 443–490
- (120) Fannes, M.; Nachtergaele, B.; Werner, R. F. Finitely Correlated Pure States. *J. Funct. Anal.* 1994, 120, 511-534.
- (121) Affleck, I.; Kennedy, T.; Lieb, E. H.; Tasaki, H. Rigorous results on valence-bond ground states in antiferromagnets. *Phys. Rev. Lett.* **1987**, *59*, 799–802.
- (122) Affleck, I.; Kennedy, T.; Lieb, E. H.; Tasaki, H. Valence bond ground states in isotropic quantum antiferromagnets. *Commun. Math. Phys.* **1988**, *115*, 477–528.
- (123) Orús, R. A practical introduction to tensor networks: Matrix product states and projected entangled pair states. *Ann. Physics* **2014**, 349, 117–158.
- (124) Strang, G. On the Construction and Comparison of Difference Schemes. SIAM J. Numer. Anal. 1968, 5, 506.
- (125) Trotter, M. F. On the Product of Semi-Groups of Operators. *Proc. Am. Math. Soc.* **1959**, *10*, 545.
- (126) Feit, M. D.; Fleck, J. A. Solution of the Schrödinger Equation by a Spectral Method II: Vibrational Energy Levels of Triatomic Molecules. *J. Chem. Phys.* **1983**, *78*, 301.
- (127) Nelson, E. Feynman Integrals and the Schrödinger Equation. *J. Math. Phys.* **1964**, *5*, 332.
- (128) Feit, M. D.; Fleck, J. A. J. Chem. Phys. 1983, 78, 301.
- (129) Feit, M. D.; Fleck, J. A. J. Chem. Phys. 1984, 80, 2578.
- (130) DeVries, P. Fast Fourier Transform Techniques in Numerical Simulations of Intense Pulse-Molecule Interactions. *Atomic and Molecular Processes with Short Intense Laser Pulses*. Bandrauk, A. D.,

- Ed.; NATO ASI Series B; Physics; Plenum Press, New York, 1988; Vol. 171; p 481.
- (131) Kosloff, D.; Kosloff, R. J. Comput. Phys. 1983, 52, 35.
- (132) Kosloff, D.; Kosloff, R. J. Chem. Phys. 1983, 79, 1823.
- (133) Kosloff, R. Propagation Methods for Quantum Molecular Dynamics. *Annu. Rev. Phys. Chem.* **1994**, *45*, 145.
- (134) Hartke, B.; Kosloff, R.; Ruhman, S. Chem. Phys. Lett. 1986, 158, 223.
- (135) Neuhauser, D. Time-Dependent Reactive Scattering in the Presence of Narrow Resonances: Avoiding Long Propagation Times. *J. Chem. Phys.* **1991**, *95*, 4927.
- (136) Huang, Y.; Iyengar, S. S.; Kouri, D. J.; Hoffman, D. K. Further Analysis of Solutions to the Time-Independent Wavepacket Equations of Quantum Dynamics II: Scattering As a Continuous Function of Energy Using Finite, Discrete Approximate Hamiltonians. *J. Chem. Phys.* **1996**, *105*, 927.
- (137) Arfken, G. Mathematical Methods for Physicists; Academic Press, New York, 1985.
- (138) Feynman, R. P.; Hibbs, A. R. Quantum Mechanics and Path Integrals; McGraw-Hill Book Company: New York, 1965.
- (139) Chandler, D.; Wolynes, P. G. Exploiting the Isomorphism Between Quantum Theory and Classical Statistical Mechanics of Polyatomic Fluids. J. Chem. Phys. 1981, 74, 4078.
- (140) Berne, B. J.; Thirumalai, D. On the Simulation of Quantum Systems: Path Integral Methods. *Annu. Rev. Phys. Chem.* **1986**, 37, 401
- (141) Makri, N. Feynman Path Integration In Quantum Dynamics. Comput. Phys. Commun. 1991, 63, 389.
- (142) Paeckel, S.; Köhler, T.; Swoboda, A.; Manmana, S. R.; Schollwöck, U.; Hubig, C. Time-evolution methods for matrix-product states. *Ann. Phys.* **2019**, *411*, 167998.
- (143) García-Ripoll, J. J. Time evolution of Matrix Product States. New J. Phys. 2006, 8, 305.
- (144) Vidal, G. Efficient simulation of one-dimensional quantum many-body systems. *Phys. Rev. Lett.* **2004**, 93, 040502.
- (145) Daley, A. J.; Kollath, C.; Schollwöck, U.; Vidal, G. Time-dependent density-matrix renormalization-group using adaptive effective Hilbert spaces. *J. Stat. Mech.* **2004**, 2004, P04005.
- (146) White, S. R.; Feiguin, A. E. Real-time evolution using the density matrix renormalization group. *Phys. Rev. Lett.* **2004**, *93*, 076401.
- (147) Zaletel, M. P.; Mong, R. S. K.; Karrasch, C.; Moore, J. E.; Pollmann, F. Time-evolving a matrix product state with long-ranged interactions. *Phys. Rev. B Condens. Matter* **2015**, *91*, 165112.
- (148) Dargel, P. E.; Wöllert, A.; Honecker, A.; McCulloch, I. P.; Schollwöck, U.; Pruschke, T. Lanczos algorithm with matrix product states for dynamical correlation functions. *Phys. Rev. B Condens. Matter* **2012**, *85*, 205119.
- (149) Wall, M. L.; Carr, L. D. Out-of-equilibrium dynamics with matrix product states. *New J. Phys.* **2012**, *14*, 125015.
- (150) Hochbruck, M.; Lubich, C. On Krylov Subspace Approximations to the Matrix Exponential Operator. *SIAM J. Numer. Anal.* **1997**, 34, 1911–1925.
- (151) Park, T. J.; Light, J. C. Unitary quantum time evolution by iterative Lanczos reduction. *J. Chem. Phys.* **1986**, 85, 5870–5876.
- (152) Gray, S. K.; Balint-Kurti, G. G. Quantum Dynamics with Real Wave Packets, Including Application to Three-Dimensional (J=0) D+H<sub>2</sub>  $\rightarrow$  HD+H Reactive Scattering. *J. Chem. Phys.* **1998**, *108*, 950.
- (153) Althorpe, S. C.; Fernandez-Alonso, F.; Bean, B. D.; Ayers, J. D.; Pomerantz, A. E.; Zare, R. N.; Wrede, E. Observation and Interpretation of a Time-Delayed Mechanism in the Hydrogen Exchange Reaction. *Nature* **2002**, *416*, 67.
- (154) Holzner, A.; Weichselbaum, A.; McCulloch, I. P.; Schollwöck, U.; von Delft, J. Chebyshev matrix product state approach for spectral functions. *Phys. Rev. B Condens. Matter* **2011**, 83, 195115.
- (155) Soley, M. B.; Bergold, P.; Gorodetsky, A. A.; Batista, V. S. Functional Tensor-Train Chebyshev Method for Multidimensional Quantum Dynamics Simulations. *J. Chem. Theory Comput.* **2022**, *18*, 25–36.

- (156) Haegeman, J.; Osborne, T. J.; Verstraete, F. Post-matrix product state methods: To tangent space and beyond. *Phys. Rev. B* **2013**, *88*, 075133.
- (157) Lubich, C.; Oseledets, I. V.; Vandereycken, B. Time integration of tensor trains. *SIAM Journal on Numerical Analysis* **2015**, 53, 917–941.
- (158) Frenkel, J. Wave Mechanics; Oxford University Press, Oxford, 1934.
- (159) Dirac, P. A. M. *The Principles of Quantum Mechanics*, fourth ed. ed.; The International series of monographs on Physics; Oxford University Press, New York, 1958; Vol. 27.
- (160) Kurashige, Y. Matrix product state formulation of the multiconfiguration time-dependent Hartree theory. *J. Chem. Phys.* **2018**, *149*, 194114.
- (161) Peláez, D.; Meyer, H.-D. The multigrid POTFIT (MGPF) method: Grid representations of potentials for quantum dynamics of large systems. *J. Chem. Phys.* **2013**, *138*, 014108.
- (162) Manzhos, S.; Carrington, T. Using neural networks to represent potential surfaces as sums of products. *J. Chem. Phys.* **2006**, 125, 194105.
- (163) Avila, G.; Carrington, T. Using a pruned basis, a non-product quadrature grid, and the exact Watson normal-coordinate kinetic energy operator to solve the vibrational Schrödinger equation for C2H4. J. Chem. Phys. 2011, 135, 064101.
- (164) Avila, G.; Carrington, T. Using nonproduct quadrature grids to solve the vibrational Schrödinger equation in 12D. *J. Chem. Phys.* **2011**, *134*, 054126.
- (165) Leclerc, A.; Carrington, T. Calculating vibrational spectra with sum of product basis functions without storing full-dimensional vectors or matrices. *J. Chem. Phys.* **2014**, *140*, 174111.
- (166) Campbell, J. E. On a Law of Combination of Operators (Second Paper). *Proc. London Math. Soc.* **1897**, *s1*–29, 14–32.
- (167) Baker, H. F. Further Applications of Matrix Notation to Integration Problems. *Proc. London Math. Soc.* **1901**, *s1*–34, 347–360.
- (168) Suzuki, M. Generalized Trotter's formula and systematic approximants of exponential operators and inner derivations with applications to many-body problems. *Commun. Math. Phys.* **1976**, *51*, 183–190.
- (169) Iyengar, S. S.; Jakowski, J. Quantum Wavepacket Ab Initio Molecular Dynamics: An Approach to Study Quantum Dynamics in Large Systems. *J. Chem. Phys.* **2005**, *122*, 114105.
- (170) Kumar, A.; DeGregorio, N.; Iyengar, S. S. Graph-Theory-Based Molecular Fragmentation for Efficient and Accurate Potential Surface Calculations in Multiple Dimensions. *J. Chem. Theory Comput.* **2021**, *17*, 6671–6690.
- (171) Kumar, A.; Iyengar, S. S. Fragment-based electronic structure for potential energy surfaces using a superposition of fragmentation topologies. *J. Chem. Theory Comput.* **2019**, *15*, 5769.
- (172) Pack, R. T.; Parker, G. A. J. Chem. Phys. 1987, 87, 3888.
- (173) Ricard, T. C.; Iyengar, S. S. An efficient and accurate approach to estimate hybrid functional and large basis set contributions to condensed phase systems and molecule-surface interactions. *J. Chem. Theory Comput.* **2020**, *16*, 4790.
- (174) Dey, T. K.; Shah, N. R. On the number of simplicial complexes in Rd. Comput. Geom. 1997, 8, 267.
- (175) Adams, C. C.; Franzosa, R. D. Introduction to topology: pure and applied; 2008.
- (176) Berger, M.; Pansu, P.; Berry, J.-P.; Saint-Raymond, X. Affine spaces. In *Problems in Geometry*; Springer, 1984; p 11.
- (177) Moon, J. W.; Moser, L. On cliques in graphs. Isr. J. Math. 1965, 3, 23–28.
- (178) Balas, E.; Yu, C. S. Finding a maximum clique in an arbitrary graph. SIAM J. Comput. 1986, 15, 1054–1068.
- (179) Li, J.; Iyengar, S. S. Ab initio Molecular Dynamics using Recursive, Spatially Separated, Overlapping Model Subsystems Mixed Within an ONIOM Based Fragmentation Energy Extrapolation Technique. *J. Chem. Theory Comput.* **2015**, *11*, 3978–3991.

- (180) Li, J.; Haycraft, C.; Iyengar, S. S. Hybrid, Extended Lagrangian Born-Oppenheimer *Ab Initio* Molecular Dynamics using Fragment-Based Electronic Structure. *J. Chem. Theory Comput.* **2016**, *12*, 2493. (181) Haycraft, C.; Li, J.; Iyengar, S. S. Efficient, "On-the-fly" Born–Oppenheimer and Car–Parrinello–type Dynamics with coupled cluster accuracy through Fragment Based Electronic Structure. *J. Chem. Theory Comput.* **2017**, *13*, 1887.
- (182) Ricard, T. C.; Haycraft, C.; Iyengar, S. S. Adaptive, geometric networks for efficient coarse-grained *ab initio* molecular dynamics with post-Hartree-Fock accuracy. *J. Chem. Theory Comput.* **2018**, *14*, 2852
- (183) Ricard, T. C.; Iyengar, S. S. Efficiently capturing weak interactions in *ab initio* molecular dynamics through "on-the-fly" basis set extrapolation. *J. Chem. Theory Comput.* **2018**, *14*, 5535.
- (184) Ricard, T. C.; Kumar, A.; Iyengar, S. S. Embedded, graph-theoretically defined many-body approximations for wavefunction-in-DFT and DFT-in-DFT: Applications to gas- and condensed-phase ab initio molecular dynamics, and potential surfaces for quantum nuclear effects. *Int. J. Quantum Chem.* **2020**, *120*, No. e26244.
- (185) Ricard, T. C.; Zhu, X.; Iyengar, S. S. Capturing weak interactions in surface adsorbate systems at couple cluster accuracy: study of PFOA on a water surface. *J. Chem. Theory Comput.* **2023**, *19*, 8541.
- (186) Zhang, J. H.; Ricard, T. C.; Haycraft, C.; Iyengar, S. S. Weighted-Graph-Theoretic Methods for Many-Body Corrections within ONIOM: Smooth AIMD and the Role of High-Order Many-Body Terms. J. Chem. Theory Comput. 2021, 17, 2672–2690.
- (187) Zhu, X.; Iyengar, S. S. Graph Theoretic Molecular Fragmentation for Multidimensional Potential Energy Surfaces Yield an Adaptive and General Transfer Machine Learning Protocol. *J. Chem. Theory Comput.* **2022**, *18*, 5125–5144.
- (188) Iyengar, S. S.; Saha, D.; Dwivedi, A.; Lopez-Ruiz, M. A.; Kumar, A.; Zhang, J. H.; Ricard, T. C.; Richerme, P.; Sabry, A. Quantum Algorithms for the Study of Electronic Structure and Molecular Dynamics: Novel Computational Protocols. In *Comprehensive Computational Chemistry*; Elsevier, 2023.
- (189) Dwivedi, A.; Rasmussen, A. J.; Richerme, P.; Iyengar, S. S. Quantum nuclear dynamics on a distributed set of ion-trap quantum computing systems. *arXiv preprint*. DOI: 10.48550/arXiv.2406.05197.
- (190) Hoffman, D. K.; Nayar, N.; Sharafeddin, O. A.; Kouri, D. J. Analytic Banded Approximation for the Discretized Free Propagator. *J. Phys. Chem.* **1991**, *95*, 8299.
- (191) Iyengar, S. S. Ab Initio Dynamics with Wave-Packets and Density Matrices. Theor. Chem. Accts. 2006, 116, 326.
- (192) Saha, D.; Iyengar, S. S.; Richerme, P.; Smith, J. M.; Sabry, A. Mapping Quantum Chemical Dynamics Problems to Spin-Lattice Simulators. *J. Chem. Theory Comput.* **2021**, *17*, 6713–6732.
- (193) Golub, G. H.; Loan, C. F. V. *Matrix Computations*; The Johns Hopkins University Press, Baltimore, 1996.
- (194) Chandrasekaran, S.; Ipsen, I. C. F. On Rank-Revealing Factorisations. SIAM J. Matrix Anal. Appl. 1994, 15, 592–622.
- (195) Hong, Y. P.; Pan, C.-T. Rank-revealing QR factorizations and the singular value decomposition. *Math. Comput.* **1992**, 58, 213–232.
- (196) Donald, M. J.; Horodecki, M.; Rudolph, O. The uniqueness theorem for entanglement measures. *J. Math. Phys.* **2002**, *43*, 4252–4272.
- (197) Eisert, J.; Osborne, T. J. General entanglement scaling laws from time evolution. *Phys. Rev. Lett.* **2006**, 97, 150404.
- (198) Schuch, N.; Wolf, M. M.; Vollbrecht, K. G. H.; Cirac, J. I. On entropy growth and the hardness of simulating time evolution. *New J. Phys.* **2008**, *10*, 033032.
- (199) Oseledets, I. V. Tensor-train decomposition. SIAM Journal on Scientific Computing 2011, 33, 2295–2317.
- (200) Cohen, E.; Tamir, B. D-Wave and predecessors: From simulated to quantum annealing. *International Journal of Quantum Information* **2014**, *12*, 1430002.
- (201) Cleland, W. W.; Kreevoy, M. M. Low-Barrier Hydrogen-Bonds and Enzymatic Catalysis. *Science* **1994**, *264*, 1887.

- (202) Frey, P. A.; Whitt, S. A.; Tobin, J. B. A Low-Barrier Hydrogen-Bond in the Catalytic Triad of Serine Proteases. *Science* **1994**, *264*, 1927.
- (203) Warshel, A.; Papazyan, A.; Kollman, P. A. On Low-Barrier Hydrogen-Bonds and Enzyme Catalysis. *Science* **1995**, *269*, 102.
- (204) Shin, J.-W.; Hammer, N. I.; Diken, E. G.; Johnson, M. A.; Walters, R. S.; Jaeger, T. D.; Duncan, M. A.; Christie, R. A.; Jordan, K. D. Infrared Signature of Structures Associated with the  $H^+(H_2O)_n$  (N = 6 to 27) Clusters. *Science* **2004**, *304*, 1137.
- (205) Headrick, J. M.; Diken, E. G.; Walters, R. S.; Hammer, N. I.; Christie, R. A.; Cui, J.; Myshakin, E. M.; Duncan, M. A.; Johnson, M. A.; Jordan, K. Spectral Signatures of Hydrated Proton Vibrations in Water Clusters. *Science* 2005, 308, 1765.
- (206) Hammer, N. I.; Diken, E. G.; Roscioli, J. R.; Johnson, M. A.; Myshakin, E. M.; Jordan, K. D.; McCoy, A. B.; Huang, X.; Bowman, J. M.; Carter, S. The Vibrational Predissociation Spectra of the  $H_5O_2^+$ .RG<sub>n</sub>(RG = Ar,Ne) clusters: Correlation of the solvent perturbations in the free OH and shared proton transitions of the Zundel ion. *J. Chem. Phys.* **2005**, *122*, 244301.
- (207) Diken, E. G.; Headrick, J. M.; Roscioli, J. R.; Bopp, J. C.; Johnson, M. A.; McCoy, A. B. Fundamental Excitations of the Shared Proton in the  ${\rm H_3O_2}^-$  and  ${\rm H_5O_2}^+$  Complexes. *J. Phys. Chem. A* **2005**, 109, 1487.
- (208) Iyengar, S. S.; Petersen, M. K.; Day, T. J. F.; Burnham, C. J.; Teige, V. E.; Voth, G. A. The Properties of Ion-Water Clusters. I. the Protonated 21-Water Cluster. *J. Chem. Phys.* **2005**, *123*, 084309.
- (209) Li, X.; Teige, V. E.; Iyengar, S. S. Can the Four-Coordinated, Penta-Valent Oxygen in Hydroxide Water Clusters Be Detected Through Experimental Vibrational Spectroscopy? *J. Phys. Chem. A* **2007**, *111*, 4815.
- (210) Li, X.; Moore, D. T.; Iyengar, S. S. Insights from First Principles Molecular Dynamics Studies Towards Infra-Red Multiple-Photon and Single-Photon Action Spectroscopy: Case Study of the Proton-Bound Di-Methyl Ether Dimer. *J. Chem. Phys.* **2008**, *128*, 184308.
- (211) Sumner, I.; Iyengar, S. S. Quantum Wavepacket *Ab Initio* Molecular Dynamics: An Approach for Computing Dynamically Averaged Vibrational Spectra Including Critical Nuclear Quantum Effects. *J. Phys. Chem. A* **2007**, *111*, 10313.
- (212) Knapp, M. J.; Rickert, K.; Klinman, J. P. Temperature-Dependent Isotope Effects in Soybean Lipoxygenase-1: Correlating Hydrogen Tunneling with Protein Dynamics. *J. Am. Chem. Soc.* **2002**, 124, 3865.
- (213) Vendrell, O.; Gatti, F.; Meyer, H.-D. Dynamics and Infrared Spectroscopy of the Protonated Water Dimer. *Ang. Chem. Intl* **2007**, 46, 6918.
- (214) Vendrell, O.; Gatti, F.; Meyer, H.-D. Full Dimensional (15D) Quantum-Dynamical Simulation of the Protonated Water-Dimer II: Infrared Spectrum and Vibrational Dynamics Dynamics and Infrared Spectroscopy of the Protonated Water Dimer. *J. Chem. Phys.* **2007**, 127, 184303.
- (215) Moissette, A.; Batonneau, Y.; Brémard, C. Conformation and protonation of 2,2'-bipyridine and 4,4'-bipyridine in acidic aqueous media and acidic ZSM-5 zeolites: A Raman scattering study. *J. Am. Chem. Soc.* **2001**, *123*, 12325–12334.
- (216) Vitale, M.; Castagnola, N. B.; Ortins, N. J.; Brooke, J. A.; Vaidyalingam, A.; Dutta, P. K. Intrazeolitic Photochemical Charge Separation for Ru(bpy)<sub>3</sub><sup>2+</sup> -Bipyridinium System: Role of the Zeolite Structure. *J. Phys. Chem. B* **1999**, *103*, 2408–2416.
- (217) Graetzel, M. Artificial photosynthesis: water cleavage into hydrogen and oxygen by visible light. *Acc. Chem. Res.* **1981**, *14*, 376–384.
- (218) Howard, S. T. Conformers, Energetics, and Basicity of 2,2'-Bipyridine. *J. Am. Chem. Soc.* **1996**, *118*, 10269–10274.
- (219) Steel, P. J. Aromatic nitrogen heterocycles as bridging ligands; a survey. *Coord. Chem. Rev.* **1990**, *106*, 227–265.
- (220) Kanjilal, P. P.; Palit, S.; Saha, G. Fetal ECG extraction from single-channel maternal ECG using singular value decomposition. *IEEE Transactions on Biomedical Engineering* **1997**, 44, 51–59.

(221) Press, W. H.; Teukolsky, S. A.; Vetterling, W. T.; Flannery, B. P. *Numerical Recipes in C*; Cambridge University Press, New York, 1992.